Journal of Manufacturing Processes 127 (2024) 511–530

Contents lists available at ScienceDirect

Journal of Manufacturing Processes

journal homepage: www.elsevier.com/locate/manpro

# Evaluating and correlating multimodal process dynamics, microstructure features, and mechanical properties in laser powder bed fusion

Haolin Zhang [a], Alexander N. Caputo [b], Chaitanya Krishna Prasad Vallabh [a,1], Heyang Zhang [a], Richard W. Neu [b], Xiayun Zhao [a,*]

[a] ZXY Intelligent Precision Advanced Manufacturing Laboratory, Department of Mechanical Engineering and Materials Science, University of Pittsburgh, Pittsburgh, PA 15261, USA

[b] Mechanical Properties Characterization Facility, George W. Woodruff School of Mechanical Engineering, Georgia Institute of Technology, Atlanta, GA 30332, USA

ARTICLE INFO

*Keywords:*
Powder bed fusion
Multimodal in-situ monitoring
Melt pool
Fatigue
Hardness
Grain size

ABSTRACT

Laser powder bed fusion (LPBF) in additive manufacturing holds the potential for efficiently producing high-resolution components with intricate geometries. However, LPBF-printed parts often exhibit deformation, defects, and suboptimal mechanical performance, limiting their applications in critical industries. The melt pool characteristics, spatters, and in-process layer surface properties play a crucial role in determining the microstructure formation and defect generation during LPBF, consequently affecting the properties of printed components. This work aims to develop a framework for revealing the relationships between complex LPBF process dynamics, microstructure, and mechanical properties, utilizing the authors' unique in-situ multi-sensor monitoring big data. The study investigates the relationships between process signatures—such as melt pool geometry, temperature, spatter, and layer surface features—and outcomes like grain characteristics, hardness, and fatigue life, using support vector machine regression models. It reveals the importance of acquiring and combining physically meaningful quantities like absolute melt pool temperature, spatter count, and in-process layer surface roughness for accurate part property prediction. These approaches outperform traditional intensity-based monitoring methods. The demonstrated framework of multi-sensor in-situ monitoring and multimodal feature fusion promises to significantly enhance the understanding and optimization of LPBF processes for producing advanced materials and components with sophisticated designs.

## 1. Introduction

Metal-based additive manufacturing (AM) has gained significance across various industries, including energy, aerospace, automobile, and bioengineering. Its ability to create intricate parts with ease, flexibility, and efficiency is well-recognized [1,2]. However, the practical application and widespread adoption of AM products still face challenges, primarily due to inconsistent part quality, which is closely tied to mechanical properties determined by the microstructure. Among the different metal AM technologies, laser powder bed fusion (LPBF) stands out as one of the most widely used methods, known for its good resolution and dimensional accuracy. In LPBF, a laser selectively scans and sinters or melts thin layers of fine metallic powder spread by a recoating rake on a platform to build 3D components [3]. The mechanical properties of LPBF-printed parts play a crucial role in their functionality, performance, and suitability for specific applications. However, due to the complex interactions between the laser, powder, printed layers, and processing gas, the mechanical properties of LPBF-printed parts exhibit undesired variability, making them unsuitable for industrial applications and large-scale production. As a result, there is a growing focus on studying how various factors, including powder characteristics, process parameters, and post-build heat treatments, influence properties such as strength, ductility, and fatigue life [4–6]. Understanding the relationships between the manufacturing process, microstructure, and final properties is key to optimizing LPBF processing parameters and post-processing techniques for improved mechanical properties [7–9]. Nevertheless, significant challenges remain. Fully comprehending the complex interactions between ultrafast laser-metal interactions, melt flow, solidification kinetics, and defect formation inherent to AM is a hurdle [10,11]. Another significant challenge lies in quantitatively

* Corresponding author.
*E-mail address:* xiayun.zhao@pitt.edu (X. Zhao).
[1] Current Address: Department of Mechanical Engineering, Stevens Institute of Technology, Hoboken, NJ, 07030

https://doi.org/10.1016/j.jmapro.2024.08.003
Received 25 April 2024; Received in revised form 25 July 2024; Accepted 3 August 2024
Available online 12 August 2024

analyzing the heterogeneous microstructures and mechanical properties in as-fabricated parts, which are caused by the varying thermal conditions throughout the LPBF process [12].

Researchers have made significant strides in developing computational modeling and simulation methods for AM. However, progress has been hindered by the lack of precise values for high-dimensional model parameters and limited access to high-performance computing resources [13,14]. Experimental approaches that employ various characterization techniques such as electron backscatter diffraction (EBSD), scanning electron microscopy (SEM), X-ray diffraction (XRD), and tensile and fatigue testing have also been developed. But these lengthy, expensive, and destructive techniques are limited to characterizing printed parts at very small scales. This is especially problematic when evaluating a wide range of properties such as hardness, tensile strength, elongation to fracture, impact toughness, and fatigue life at large scale [15,16].

Lately, machine learning has been employed to accelerate and enhance the prediction of part properties [17]. Models ranging from traditional random forest algorithms to deep convolutional neural networks (CNNs) are applied to predict the porosity or surface defects of LPBF-printed part [18–20]. In [21], a Gaussian process regression model is used to predict the relationship between LPBF process parameters (laser power and scan speed) and multiple properties including hardness, tensile strength, and fracture toughness. But it shows a large variation in resulting mechanical properties despite similar process parameters. Stebner's research team discovered that, despite employing build orientation and position along with machine learning algorithms, they couldn't fully account for the observed variations in mechanical properties. As a result, they proposed the need to consider additional variables to comprehensively understand the factors influencing the ultimate mechanical characteristics of LPBF-printed components [22]. More similar approaches indicate that solely using nominal process settings (e.g., laser power, speed, hatching space, layer thickness, build position) is difficult to capture the variations in process and machines for accurate predictions of printed part properties [23,24]. Therefore, the current research direction involves integrating dynamic process signatures observed through in-situ monitoring to enhance the modeling of process-structure-property relationships. While many works are focused on predicting defects such as porosity and geometrical properties, there is limited information available regarding the direct prediction of mechanical properties using in-situ monitoring data [25–28].

Among the various mechanical properties of LPBF-printed parts, fatigue performance holds particular importance because it directly impacts the long-term durability and safety of AM components. Traditional experimental tests used to assess the fatigue strength of printed parts are both costly and time-consuming. While simulation-based methods have been developed to estimate stress distribution and material behavior during cyclic loading and predict fatigue life, their accuracies remain limited. To address this challenge, researchers have explored the influence of process conditions, such as laser power, build orientation, and post-processing, on the fatigue behavior of LPBF parts utilizing machine learning techniques [29,30]. However, it is essential to note that the current state of research in predicting fatigue strength in LPBF is still in its early stages, requiring further exploration to gain a comprehensive understanding of the intricate relationships. This understanding should encompass not only the nominal process input parameters but, more significantly, the real process dynamics and the microstructure of as-printed parts, both of which impact fatigue behavior.

While it would be ideal, performing a full-scale simulation or conducting a comprehensive characterization of an entire LPBF process is exceedingly challenging for accurately predicting the properties of printed parts. It is known that melt pool (MP) properties, along with issues like spatters and surface roughness, play a crucial role in determining the microstructure formation and the generation of defects during LPBF, which, in turn, affect the properties of the printed parts. Currently, there is a notable lack of research on comprehensive LPBF monitoring and the fusion analysis of data from multiple sensors to predict mechanical properties. The primary aim of this research is to utilize in-situ monitored data, which includes features like melt pool temperature, area, intensity, spatter, and layer-wise surface roughness, to predict mechanical properties that are characterized ex-situ, such as fatigue life and Vickers hardness. The goal is to establish a robust correlation between the entire process and the resulting properties, shedding light on the potential of in-situ process signatures to uncover any anomalies present in the printed parts. Ultimately, the proposed framework of machine learning of multi-monitoring data can be used to enhance the understanding of the LPBF process-multi-properties relationships and facilitate the optimization and control of LPBF processes for achieving improved mechanical properties.

The structure of the paper is divided into the following. The experiment design with materials and processing parameters selection are introduced in Section 2.1. In-situ monitoring systems setup including a coaxial single-camera two-wavelength imaging pyrometry (Section 2.2.1), off-axis high-speed camera-based spatter monitoring (Section 2.2.2), and in-situ fringe projection profilometry method for layer-wise surface topography monitoring (Section 2.2.3) are elaborated. Details on post-build heat treatment, high-cycle fatigue testing, microstructure characterization through EBSD analysis, fractography imaging, and hardness testing are presented in Section 2.3. All the experiment results are presented and discussed in Section 3. In Section 3.1, in-situ monitored MP signatures are presented and compared among samples whereas the in-situ measured surface topography and resulting surface roughness are discussed in Section 3.2. Characterized fatigue lives and hardness value are presented in Section 3.3 with discussions on the potential causes of the observed difference of mechanical properties among samples. The EBSD analysis is also utilized in Section 3.4 to reveal the process dynamics and variations. Finally, regression models and analysis are performed in Sections 3.5 and 3.6 to study and compare the importance of different features in correlating to the characterized ex-situ mechanical properties.

## 2. Materials and methods

### 2.1. LPBF experiment: sample printing and process monitoring

As an initial study case, five fatigue testing bars designed based on ASTM E466 standards are printed using Inconel 718 powders (VDM® Alloy 718, Werdohl, Germany) and a commercial LPBF machine of EOS M290 DMLS (Direct Metal Laser Sintering). The default EOS printing parameters for Inconel 718 were employed (laser power: 285 W, laser scan speed: 960 mm/s, layer thickness: 40 $\mu$m) along with a hatch spacing of 110 $\mu$m with 67° rotation and 10 mm strip width. The position of the five samples on EOS M290 built plate and their design geometry are shown below in Fig. 1 with the printing order indicated by the blue arrow. The IN718 powder used was sieved with the 80 $\mu$m vibrating sieve that is embedded into the EOS printer. The standard contouring scan (laser power: 80 W, and laser scan speed: 800 mm/s) is implemented after laser hatching.

### 2.2. In-situ multi-sensor multimodality process monitoring

An overview of our relatively comprehensive multimodality in-situ LPBF process monitoring system is shown in Fig. 2. It includes: 1) a lab-designed single-camera two-wavelength imaging pyrometry (STWIP) system for coaxial melt pool monitoring; 2) an off-axis camera-based laser scan monitoring system for melt pool registration and spatter tracking; and 3) an in-house fringe projection profilometry (FPP) system for layer surface topography measurement.

#### 2.2.1. Single-camera two-wavelength imaging pyrometry for high-speed coaxial monitoring of melt pool temperature and morphology

This print is monitored using our developed in-situ STWIP system at a frame rate of 30,000 fps with a resolution of 128 × 48 pixels for 43

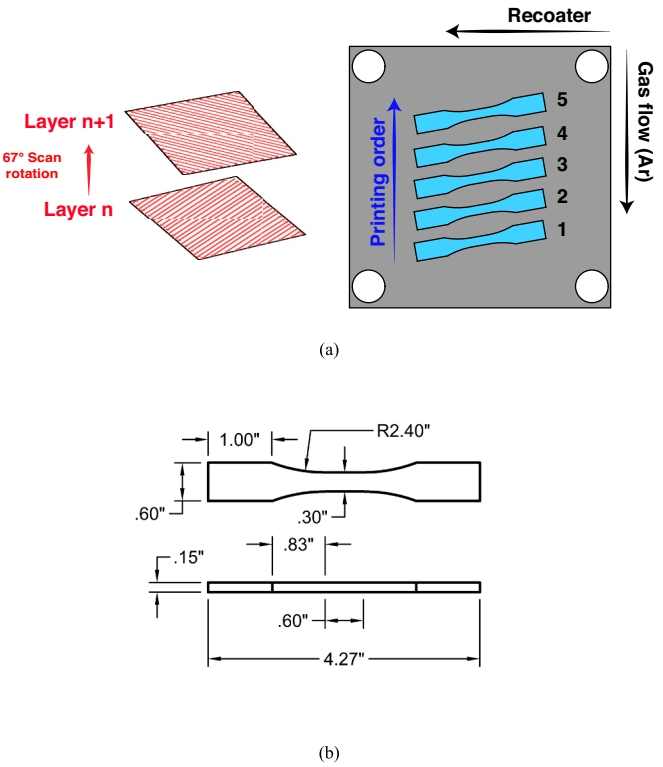


**Fig. 1.** Experiment design. (a) The printing position of five sample fatigue testing bars on EOS M290 build plate. (b) Fatigue sample geometry made in accordance with ASTM E466, with dimensional labels in inches for concision.

printed layers. Each print layer elapses 72 s with approximately 2.2 million images per layer, therefore over 1 billion images are monitored and processed for the whole monitored print. The data metrics obtained from this monitoring are MP intensity, MP area calculated by considering all the pixels with temperature above the liquidus temperature of the printing material, MP shape (ellipticity, width, and length), and MP temperature calculated through Wien's approximation of Planck's law using intensities under two wavelengths [31]. The two wavelengths used in this work are 520 nm and 620 nm wavelengths based on the optical design of the pyrometer. Details about such large-scale, continuous, high-speed monitoring using STWIP system and corresponding methods are based on previous publication [32]. Specific results of the analyzed melt pool signatures for this experiment are reported in Section 3.1.

#### 2.2.2. *Melt pool registration and spatter monitoring via an off-axis camera*

This work employs an off-axis high-speed camera to capture both the spatial location of melt pool and the spatter phenomena, allowing for the registration of the STWIP-measured melt pool signatures and the tracking of spatter signatures. The camera (FASTEC IL5Q, Fastec Inc. San Diego, CA) is placed outside the build chamber, facing the build plate at an oblique angle to observe the print process. The camera is equipped with a 6 Megapixel lens with a focal length of 25 mm (1–24,422, Navitar, Rochester, NY). It is worth noting that both the in-situ coaxial STWIP camera and the in-situ off-axis camera are synchronized using a 5 V TTL trigger signal. The off-axis camera is used to monitor the LPBF laser scans for 43 layers with a frame rate of 1000 fps (frames per second) and a resolution of 640 × 512 pixels across the build plate with a field of view of 200 mm × 180 mm. The coordinates of the STWIP monitored melt pools are derived followed by a registration of all the STWIP-measured melt pool signatures using methods reported in [33]. The spatter monitoring, measurement, and registration methods based on semantic segmentation deep learning model have been developed and reported in previous publication [34] and used to monitor and characterize the ejected spatters with a size of ~100 μm. A convolutional neural network (CNN) is trained to segment the captured images to quantify the spatter counts. In this work, 1000 manually pixel-wise labelled melt pool images with spatters are used to train, validate, and test the neural network. The dataset is split into 70 % for training, 10 % for validation, and 20 % for testing. With these methods, layer-wise feature profiles of the STWIP-measured melt pool geometrical and thermal properties as well as the off-axis observed spatters counts associated with the monitored melt pools are obtained. These multi-modality feature profiles are then utilized to investigate how these factors influence the properties of as-printed parts. The results are presented in Section 3.

#### 2.2.3. *In-situ fringe projection profilometry*

In this work, a LPBF-specific FPP system and method developed by the authors' group are implemented to measure the in-situ printed layer's surface topography with reference to the powder surface [35]. Specifically, an in-house FPP system comprises a digital, optical projector (LightCrafter 4710 EVM G2, Texas Instruments, Dallas, TX) with a resolution of 1920 × 1080 pixels and a 12 Megapixel CMOS camera (FL3-U3-120S3C-C, Flea3, Tele-dyne FLIR, Wilsonville, OR), which are synchronized by a computer-based control unit. The high dynamic range (HDR) FPP method is employed to address the issues of shadowing and intensity saturation caused by the varying material properties in LPBF. This method involves projecting two sets of sinusoidal fringes with different maximum intensities, specifically 160 and 250 grayscale values, onto the build plate. For enhanced measurement accuracy, the acquired images are fused by averaging and processed using a modified FPP sensor model that features localized camera imaging intensity correction, masked Fourier filter-aided unwrapping, and pixel-wise phase-height calibration [35]. Standard three-step phase shifting algorithm and a linear phase-height calibration model are used. Details of the implementations are shown in Appendix A.1. In-situ FPP measurement results for this experiment are presented in Section 3.2.

To prepare or encode the measured surface topography for correlation analysis, data pre-processing techniques are incorporated to extract representative features. The directly obtained signature from the FPP monitoring is areal surface roughness ($S_a$), which is the arithmetic mean of the surface deviation from main profile. $S_a$ is the overall indicator to the quality of the printed layer. However, the metric does not provide insights in the distribution and quantity of measured points/pixels with abnormal height. K-means, an unsupervised clustering algorithm, supports efficient feature extraction from given parameters by optimizing the placement of centroids of clusters to separate the data points in the training parameter space. Therefore, another representative surface metric - "Count of Abnormal Surface Features" is derived through the K-means classification of the FPP-measured surface topography and utilized for evaluating printed part properties. Specifically, before applying the K-means, the surface topography is first filtered through the average convolution layer since the rough and anomalous pixels are primarily identified based on the pixels surrounding them with kernels of sizes 5, 10, 15, and 50. The zero-padding filter acts as a moving average for each individual pixel to incorporate the surrounding pixel values to the K-means training. After the averaging operation, a binary K-means cluster algorithm is applied to individual layers to identify the rough pixels [36].

### 2.3. *Sample preparation, testing, and characterization*

#### 2.3.1. *Sample heat treatment procedure*

After being removed from the build plate without any stress relief heat treatment, all samples undergo a direct age heat treatment protocol prior to any characterization or mechanical testing. This procedure is chosen specifically to preserve the microstructure resulting from the AM build conditions. It is similar to AMS 5662 and consisted of two stages in a tube furnace in an Argon atmosphere: first, 720°C for 8 h then, furnace

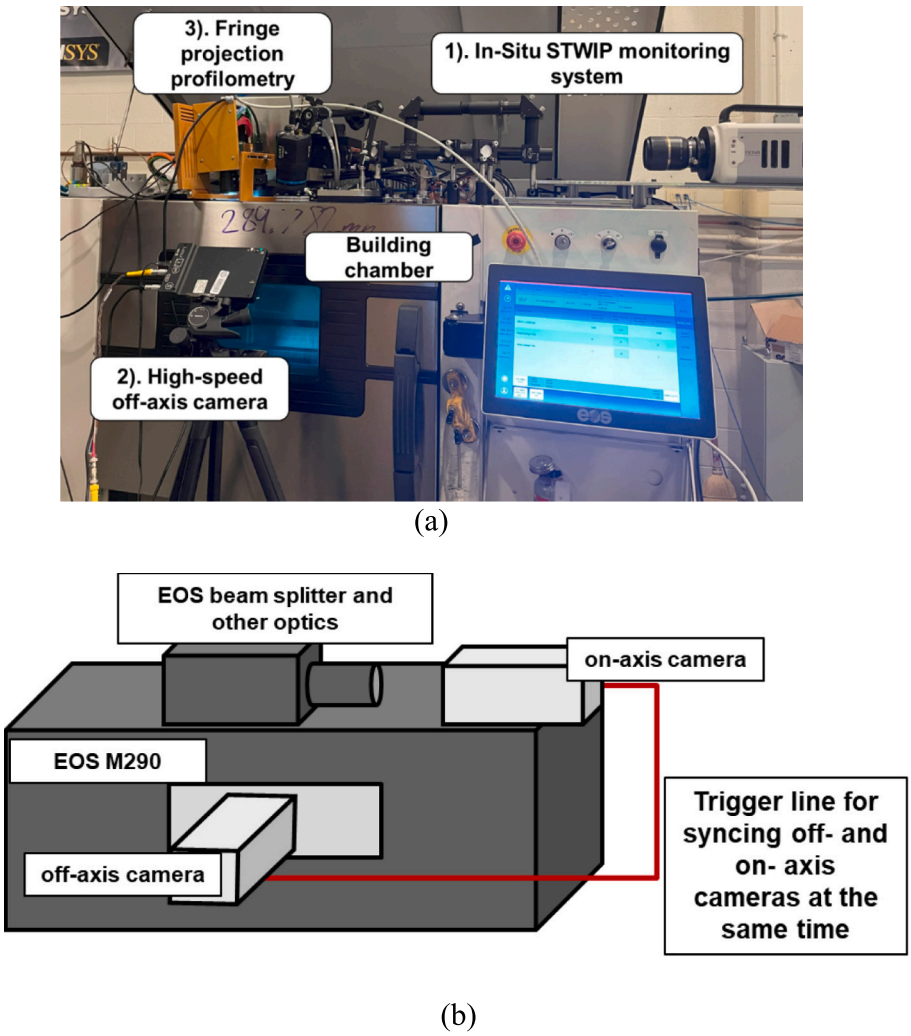


**Fig. 2.** Our in-situ multi-sensor multimodality LPBF process monitoring system: (a) physical setup; and (b) schematic of the coaxial STWIP camera and off-axis camera which are synchronized.

cooled to 620°C and held for 8 h prior to being removed and air cooling to room temperature in lab air.

*2.3.2. High cycle fatigue testing and fatigue fracture characterization*

All testing in this work is conducted in force control on an MTS model 370 servohydraulic test system (Eden Prairie, MN, USA). Samples are gripped using hydraulic wedge grips with serrated steel inserts using 1/16″ thick garolite shims to prevent fatigue samples from fracture in the grip sections. Guides are used to insure alignment of fatigue samples between the wedge grips. The guides are installed using a flat calibration sample and a level to insure vertical alignment of fatigue samples. The high cycle fatigue (HCF) test conditions comprise a stress ratio ($R$) of 0.1, a maximum stress ($\sigma_{max}$) of 500 MPa, and a loading frequency of 20 Hz with a sinusoidal wave form in room temperature lab air.

Fracture surface analysis of all samples is conducted to identify the location of the critical defect. SEM imaging is performed on a Thermo Scientific Phenom XL G2 scanning electron microscope. Samples are sonicated in an acetone bath and cleaned with pressurized air prior to being inserted into the SEM. An accelerating voltage of 10 kV is used for imaging using a secondary electron detector in the Phenom SEM.

*2.3.3. Microstructure characterization*

After the HCF testing, part of the filleted region of each of the five samples are sectioned out, mounted, and polished from 180 grit down to a 0.04 μm colloidal alumina slurry to create a mirror finish free of scratches. The exact brand used in this work for the final surface finish is the Struers OP-U colloidal alumina. From each fatigue sample, three orientations are obtained. The XY, YZ, and XZ orientations, as related to the sample coordinate axes, are depicted in the schematic from Fig. 3. For each of the five fatigue samples, six EBSD maps are taken at various adjacent locations in each of the three orientations using a TESCAN Mira FE-SEM. To obtain the EBSD patterns, an EDAX Velocity EBSD camera (Mahwah, NJ) is used along with the TEAMS software by EDAX. An acceleration voltage of 20 kV is employed along with working distances between 20 mm and 27 mm. All EBSD data is processed using the ATEX software.

*2.3.4. Hardness testing*

Vickers hardness testing is conducted in accordance with ASTM E384 on the grip regions of all samples (polished up to 400grit) using a LECO LM248AT Microhardness Tester with 500 gf weight applied. Each sample is indented 20 separate times and all indentations are measured

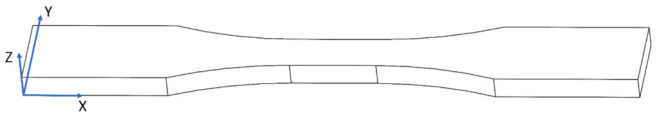


**Fig. 3.** Schematic depicting the sample coordinate system in microstructure characterization.

using the integrated optical microscope of the LECO LM248AT system.

## 3. Results and discussions

### 3.1. Multimodality melt pool properties obtained from our unique concurrent in-situ STWIP and off-axis camera monitoring systems

#### 3.1.1. Melt pool surface temperature and geometrical properties

The coaxial STWIP-monitored MP signatures including MP temperature, MP area, and MP width, are registered, respectively, with the off-axis camera monitored spatial coordinates to form comprehensive layer-wise MP signature maps (MPSMs). Due to the frequency difference between the STWIP (30,000 fps) and the off-axis camera (1000 fps), linear interpolation is applied to estimate the spatial coordinates of MPs that are not directly monitored by the off-axis camera. This is done by fitting the linear curve using coordinates of every two consecutive MPs observed by the off-axis camera, and further inserting the MPs monitored by the STWIP camera uniformly into the range. Representative layer-wise profiles of melt pool signatures (i.e., MPSMs) are shown in Fig. 4.

Shown in Fig. 4, the processing transition, resulting from a change in machine parameters between filling and contouring, can be readily observed in MPSMs through temperature drops and variations in the area. To comprehensively observe the variations of melt pool-level signatures monitored by the high-speed STWIP (measurement frequency: 30,000 Hz), layer-wise high-resolution signatures including MP average temperature, MP area and average intensity at the two wavelengths used by STWIP - 620 nm and 550 nm, respectively, are calculated. Because the MP area and intensity monitored under the two wavelengths in STWIP are highly correlated, for efficiency only the melt pool area and average intensity measured under 620 nm wavelength are used in the following analysis. Results for layer-wise signatures used in subsequent correlation analysis (Sections 3.4–3.6) are shown in Fig. 5, and the standard deviations are plotted as error bars. It is observed that generally Sample 3 and Sample 4 exhibit higher average MP temperature across all the layers monitored comparing to Samples 1, 2, and 5. Based on the IN718 single-track experiment results reported from [37], tracks printed using keyhole process setting result in the temperature around 3500 °C while tracks printed using transition or default process setting have the temperature of 3000 °C. For the fatigue bars printed in this work, the temperature difference among samples is about 400 °C, indicating a possible processing regime transition from the planned default regime to keyholing regime instead. It should be noted that the temperature difference observed among samples are not well reflected by the intensity scale monitored as the temperature is computed based on the intensity ratio (Fig. 5(d)). This also indicates that the traditional intensity-based monitoring methods are less effective compared to the newly developed STWIP method in capturing variations in the LPBF process.

#### 3.1.2. Melt pool surface temperature gradient

The MP temperature gradients for the five fatigue bars are computed using the registered MPSMs as illustrated in Fig. 4. These temperature gradients are primarily aimed to capture and reveal the spatial variations in MP surface temperature across the three directions ($x$, $y$, $z$). To calculate the gradient, the MP point cloud is organized into a grid format first with each grid covering an area of 100 μm × 100 μm (Fig. 6). After discretizing the point clouds into grid format, temperature gradients in three directions ($\frac{dT}{dx}, \frac{dT}{dy}, \frac{dT}{dz}$) were determined. Since the MP temperature being monitored is the MP surface temperature, the gradient in $z$ direction is approximated using the nominal layer thickness (40 μm) as $dz$.

The temperature gradient results for Sample 2 at layer 40 are presented in Fig. 7. Indicated by the temperature gradients in the $x$ and $y$

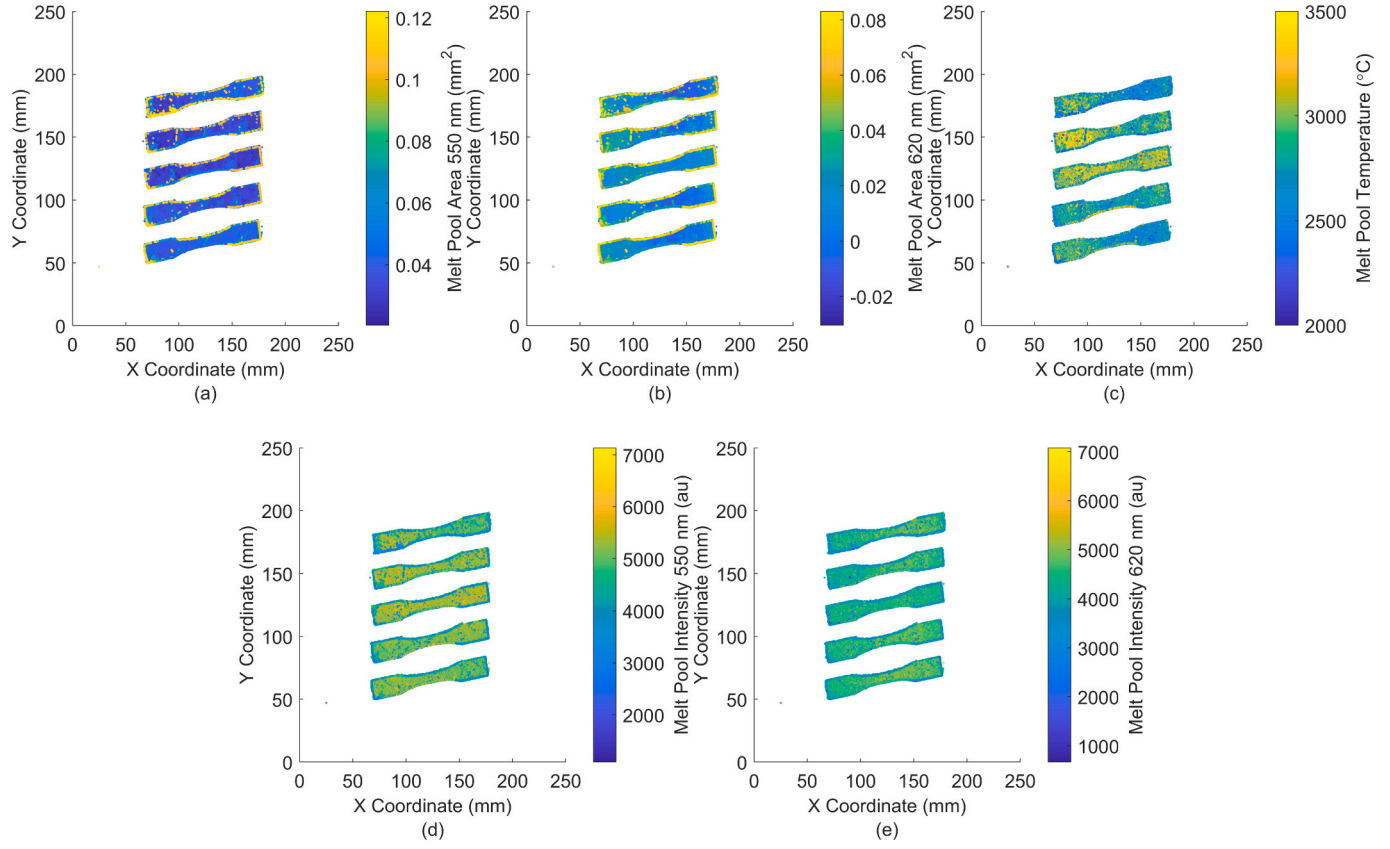


**Fig. 4.** Multimodality melt pool signature maps (MPSMs) measured and registered by our STWIP (30 kHz) in conjunction with the off-axis camera laser scan tracking, including melt pool area, average intensity measured at two wavelengths (550 nm and 620 nm), and average temperature.

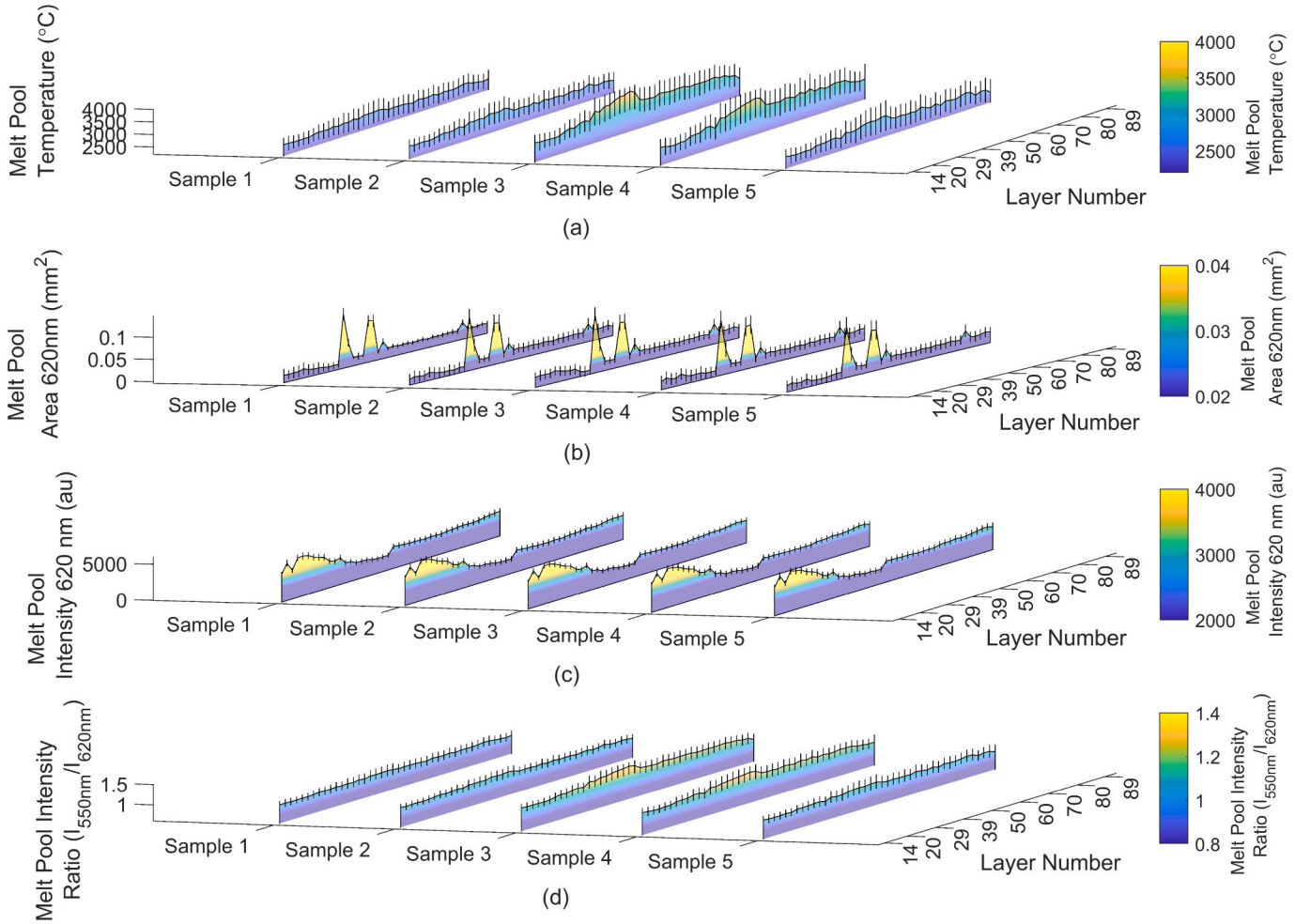


**Fig. 5.** Layer-wise melt pool signatures measured by STWIP for all the 43 monitored layers across the five samples: (a) melt pool average temperature; (b) melt pool area monitored at 620 nm; (c) melt pool intensity monitored at 620 nm; (d) melt pool intensity ratio (High temporal resolution: 1/30,000 s).

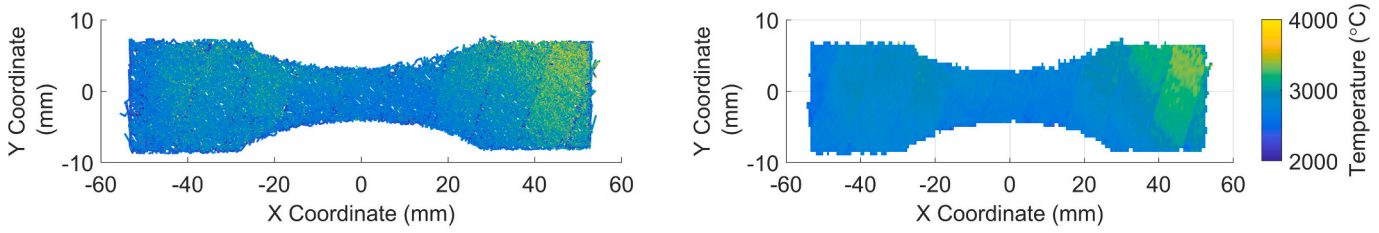


**Fig. 6.** A representative melt pool average temperature map in a point cloud format with each scatter representing individual melt pool (left) converted to a grid format with 100 $\mu$m × 100 $\mu$m grid resolution (right) for melt pool temperature gradient estimation.

directions, temperature variations are predominantly observed at the scan stripe locations where the laser is switched off at the end of each scan track. Moreover, noticeable temperature fluctuations occur at the sample's edges due to the contouring scans that adopt lower laser power and faster scan speed.

To illustrate the dynamic changes in temperature gradients across the five monitored samples, the layer-wise melt pool average surface temperature gradients were calculated for each sample in three directions. As shown in Fig. 8, the temperature gradients in these three directions are generally positive, which can be attributed to the heat accumulation during the LPBF printing process. Notably, Samples 3 and 4 exhibit more pronounced temperature variations compared to Samples 1, 2, and 5. These localized temperature fluctuations can be linked to abnormal heat accumulation resulting from process defects or irregular process behavior induced by factors such as gas flow and spattering. These process signatures of thermal gradients are utilized as inputs to correlate with the ex-situ characterized properties in the subsequent sections to further investigate the relationship between these localized temperature variations and the printed parts' mechanical properties.

### 3.1.3. *Melt pool spatter quantification*

As introduced in Section 2.2.2, a DeepLabV3 CNN was trained using the dataset with 1000 manually labelled images to process the off-axis camera-acquired melt pool images and extract spatters. The training and validation histories are shown in Fig. 9, with the highest validation accuracy achieved at 99.14 % during iteration 144. The model with highest validation accuracy was saved and tested on an unseen test dataset, yielding a test accuracy of 99.18 %. Sample results for the

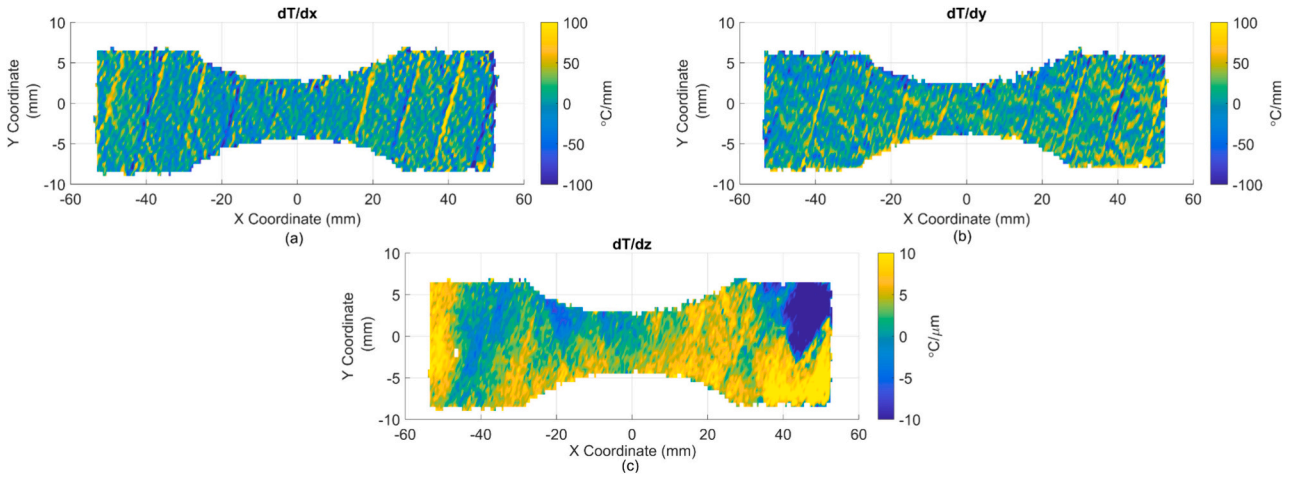


**Fig. 7.** Melt pool average surface temperature gradients for Sample 2 monitored at layer 40 in three directions. (a) $\frac{dT}{dx}$, (b) $\frac{dT}{dy}$, and (c) $\frac{dT}{dz}$.

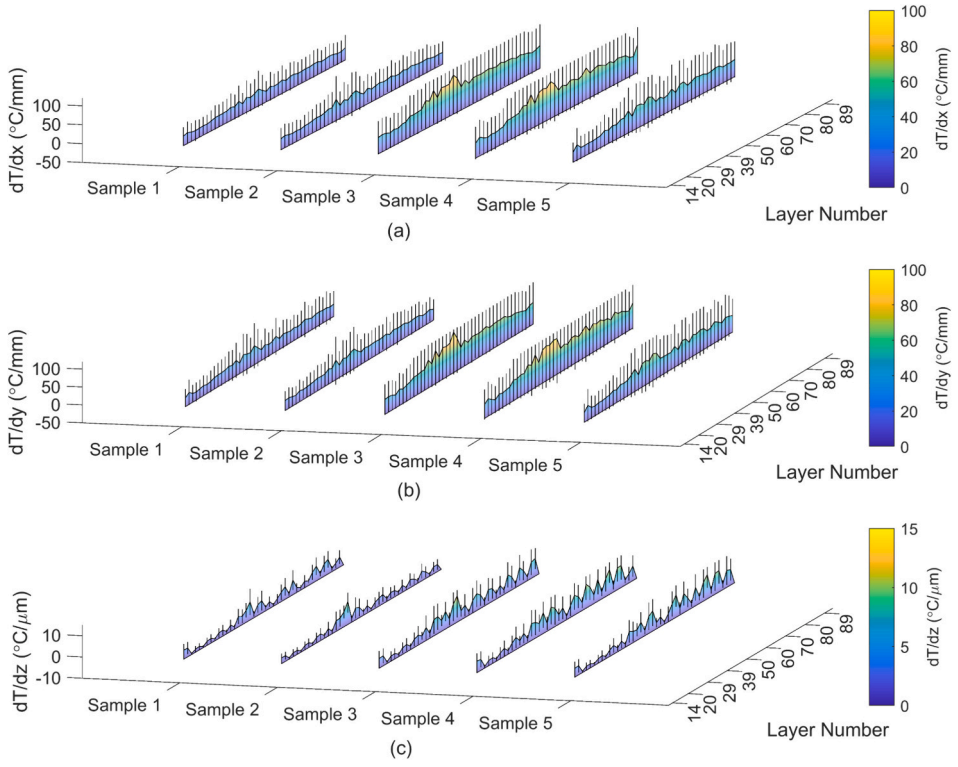


**Fig. 8.** Layer-wise average surface temperature gradients of the melt pools in the *x*, *y*, and *z* directions for all the monitored 43 layers across the five samples.

registered melt pool spatter count of six monitored layers are displayed in Fig. 9(c). These results reveal variations in spatter counts across different layers, influenced by different hatching scan angles. Additionally, the small number of spatters observed on the contour of the fatigue bars suggests a correlation between spatter occurrences and nominal processing parameters such as laser power and scan speed.

To comprehensively understand the spatter dynamics throughout the layers in this LPBF printing experiment, the layer-wise average spatter counts for all the monitored 43 layers are plotted and presented in Fig. 10. The average spatter counts in this work are defined as the average number of spatter ejections per image frame from the complete layer. It can be observed that the spatter counts for Sample 3 and 4 are notably higher compared to the spatter counts from Samples 1, 2, and 5. This observation aligns with the high temperatures observed for Sample 3 and Sample 4 using the STWIP, hinting at potential changes in the processing regime.

### 3.2. *In-process layer surface topography measured by our in-situ FPP*

The layer-wise in-process surface topography was calculated using the in-situ FPP system and methods as introduced in Section 2.2.3. The three-step phase shifting algorithm, two-dimensional Fast Fourier Transform for height map filtering, along with the measurement result of final filtered surface height map are presented in Appendix A. From the layer surface topography, the areal surface roughness (*Sa*), which is the arithmetic mean of the surface deviation from mean profile, is computed as a metric of the layer-wise surface quality. Fig. 11 shows the layer-wise average surface roughness value for all the 43 layers monitored by the in-situ FPP across all the five samples.

Detailed in Section 2.2.3, the binary K-means classification is applied

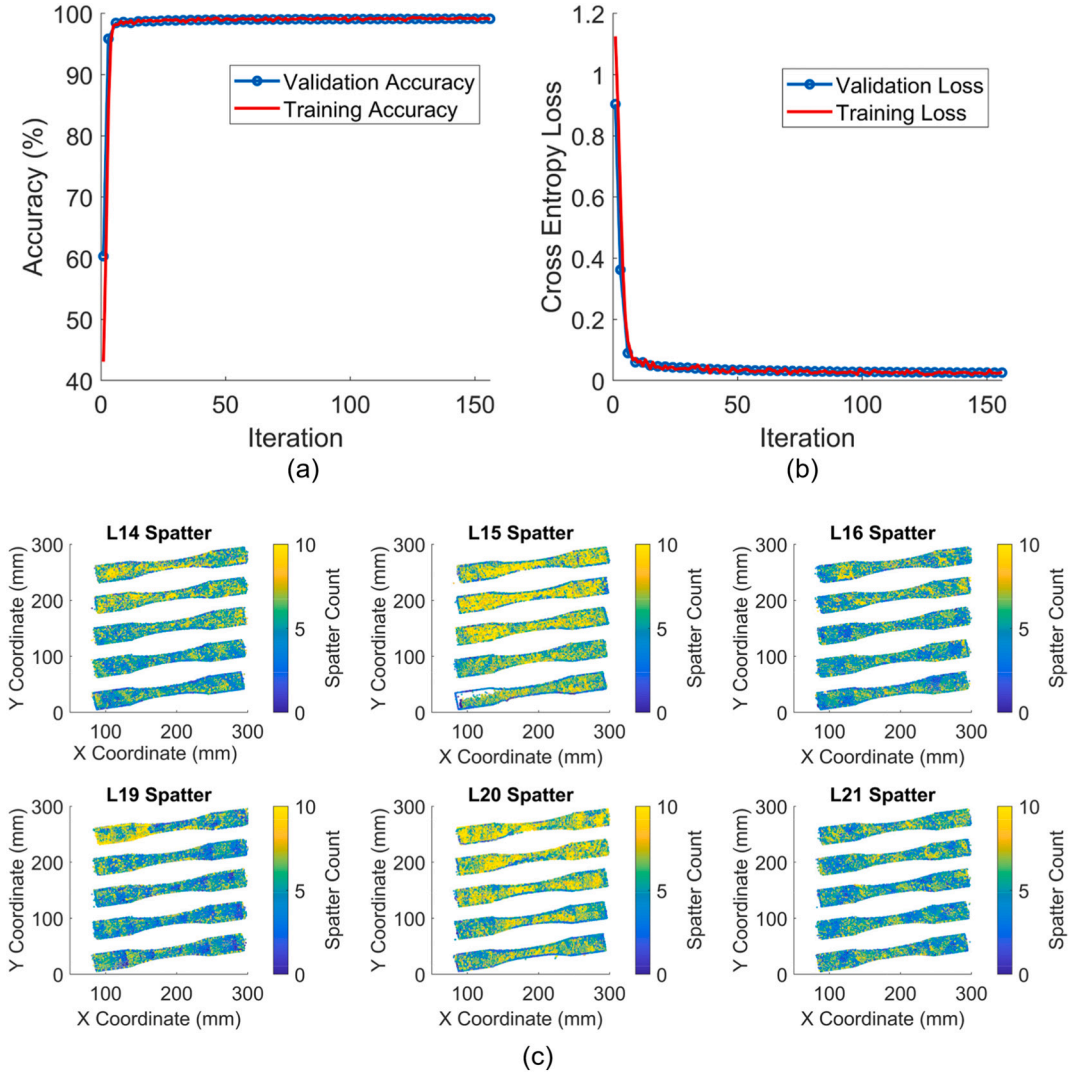


**Fig. 9.** Machine learning-aided spatter measurement and registration. (a) training and validation accuracy history. (b) training and validation loss histories. (c) sample results of spatter count map for six monitored layers.

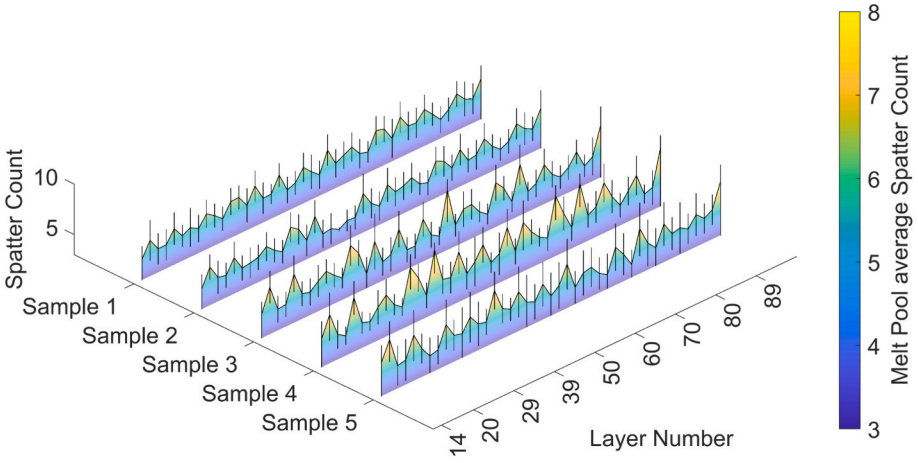


**Fig. 10.** Layer-wise average spatter count for all the monitored 43 layers across the five samples.

to extract the abnormal surface topography. The overall data processing workflow is presented in Appendix B Fig. B-1.

Furthermore, referring to Appendix Fig. B-2, Sample 4 is observed to have the most abnormal surface features based on the results of K-means unsupervised learning of the FPP-measured layer surface topographies. This observation helps clarify why Sample 4 displays one of the shortest

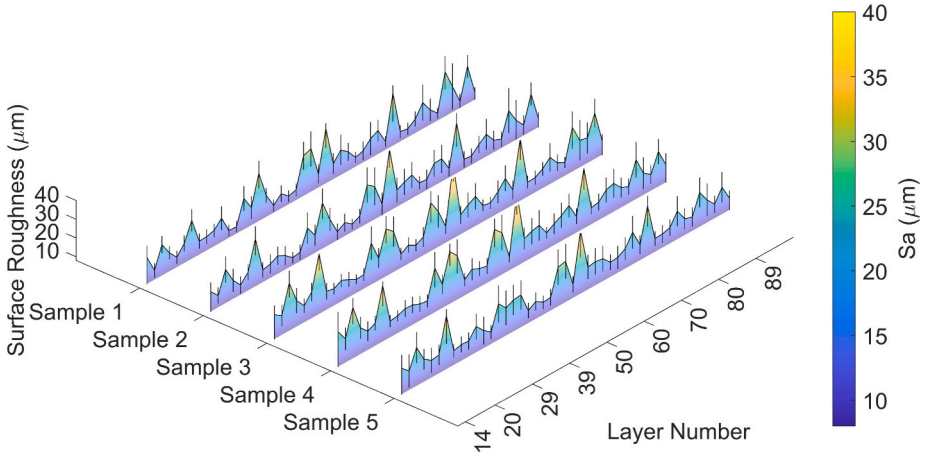


**Fig. 11.** Layer-wise surface roughness for all the monitored 43 layers across the five samples.

fatigue lives and the smallest hardness value compared to the other four samples as detailed in Section 3.3. However, when we solely consider the count of abnormal surface features, it becomes challenging to explain why Sample 1, with much fewer abnormal surface features than Sample 5, demonstrates a similar fatigue life. For this reason, a more comprehensive set of process signatures is required to accurately assess the printed part properties. Further quantitative analyses are presented in the subsequent sections, where both the metrics of surface roughness and the count of abnormal surface features, in conjunction with the melt pool signatures derived in Section 3.1, are correlated with the mechanical properties presented in Section 3.3.

### 3.3. *Ex-situ testing and characterization results*

Following the testing and characterization protocols specified in Section 2.3, mechanical properties including fatigue strength and Vickers hardness value are measured, and EBSD maps are obtained for the five printed samples. Shown in Table 1, even though the five fatigue samples are manufactured under identical nominal processing pedigree, the fatigue lives vary by more than a factor of two, from ~4 million to 9 million cycles, indicating that process variations among samples directly impact their fatigue behavior. The subsequent measurements of hardness value (HV) are conducted by using the LECO, and the results are displayed in Table 1. The average hardness values for each sample show a strong correlation with the fatigue strength, as higher HV corresponds to longer fatigue lives. Both fatigue lives and hardness values indicate that Samples 3 and 4 have degraded mechanical properties. Referring to the in-situ monitored signatures presented in Sections 3.1 and 3.2, the observation from ex-situ characterized mechanical properties qualitatively correlate with the in-situ monitored melt pool level properties and layer-wise surface properties. The elevated melt pool temperatures, temperature gradients, and rougher surfaces, accompanied by an increased count of ejected spatters, particularly as observed in Samples 3 and 4, provide strong indicators of potential defects such as keyhole-induced porosity and alterations in microstructure like grain size (refer to Section 3.4). These observations offer a plausible explanation for the comparatively weaker mechanical strength observed in the ex-situ testing of these samples.

**Table 1**
Vickers hardness values with standard deviations and fatigue lives for all samples.

| Sample | Vickers hardness [HV] | Fatigue life [$10^6$ cycles] |
|---|---|---|
| 1 | 491.3 ± 24.5 | 7.12 |
| 2 | 500.4 ± 11.4 | 9.30 |
| 3 | 482.8 ± 13.0 | 4.51 |
| 4 | 487.2 ± 15.1 | 4.00 |
| 5 | 490.2 ± 9.7 | 7.80 |

In order to understand the difference in fatigue life, ex-situ SEM-based fractography is employed to identify the fatigue critical feature or features in the fracture surface of each broken specimen. To further explain the variance in fatigue behavior, EBSD and SEM analyses are conducted on polished sections of the gage regions of each sample to elucidate any microstructural differences between samples.

From fractographic analysis, the region of each fatigue sample responsible for initial fatigue crack growth is identified using the radial cracking patterns extending from pores and/or crystallographic features. These regions coincide with the edges of the fracture surfaces that exhibited the least amount of plastic deformation prior to failure which is indicative of fatigue initiation. In Fig. 12, and detailed in Fig. 13, the regions and critical features contributing to fatigue failure in each specimen are identified. Samples 1 and 5 (Fig. 13) exhibit spherical keyhole pores (marked with yellow arrows) and large areas of mostly smooth transgranular crack growth (highlighted with yellow ovals). These especially smooth transgranular crack growth regions contrast with the more stereotypical transgranular crack growth extending from the nucleation site and are understood to be locally vulnerable crystallographic orientations in especially large grains with slip planes easily activatable by the loading of the samples. The pores present in close proximity to these very flat and angular regions of transgranular crack indicate that crystallographic microstructure and porous microstructure in these specimens contribute to the fatigue behavior. In Samples 3 and 4, which have the shortest fatigue lives, the fracture surfaces contain multiple large pores in close proximity and minimal regions of smooth transgranular crack growth. In these samples large keyhole pores near the surface and in close proximity to one another appear to be responsible for the decremented fatigue live. In the fracture surface of Sample 2, there is a ridgelike feature separating the regions shown by the solid and dashed outlines. This feature indicates that there are cracks growing from separate nucleation sites that grow into each other. This type of competitive growth ends up resulting in a longer fatigue life for Sample 2. It can be seen in the upper region with the solid yellow outline there is a region of smooth transgranular crack growth where cracks appear to be initiating, whereas in the dashed yellow outline image, a pore can be observed near the surface with cracks extending downwards from it. It is the combination and competition between these crack nucleation sites that likely provides the increased fatigue life in this specimen.

Through the SEM-based EBSD and microstructure analysis, and further confirmed by the fractographic analysis, it is observed that small keyhole porosities exist near the edges of all samples. Edges in this case are defined as the regions in each sample where the laser tracks turn around, which is known to form keyhole porosity, and where the

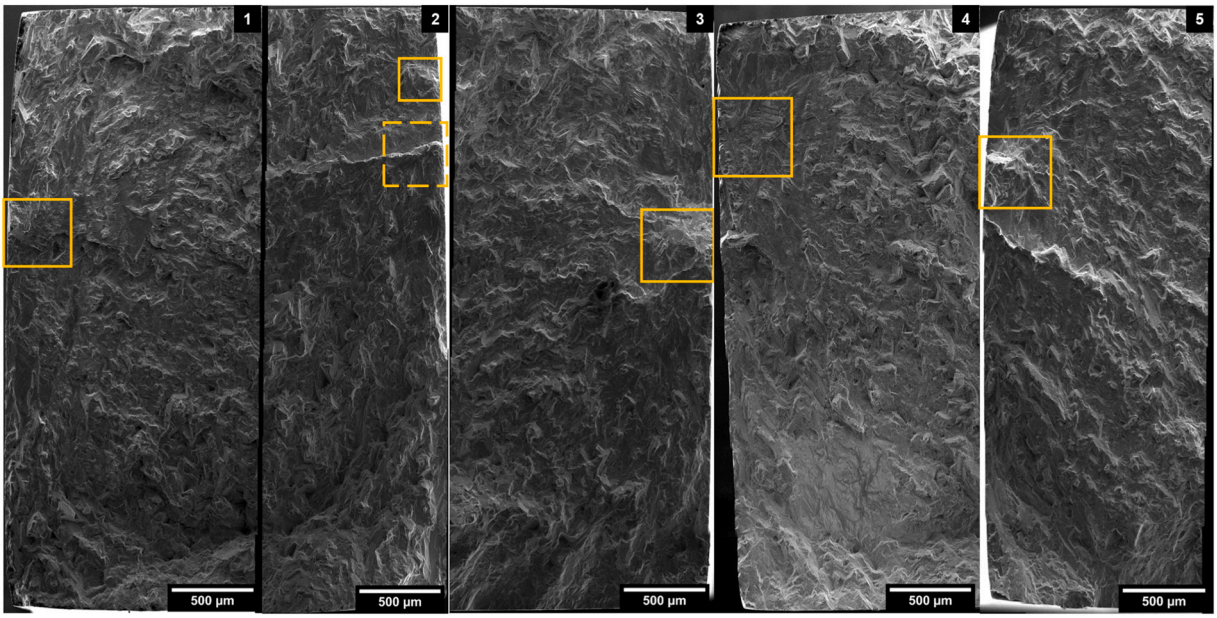


**Fig. 12.** Stitched SEM fractography images of all samples with critical defect locations outlined and further detailed in Fig. 13.

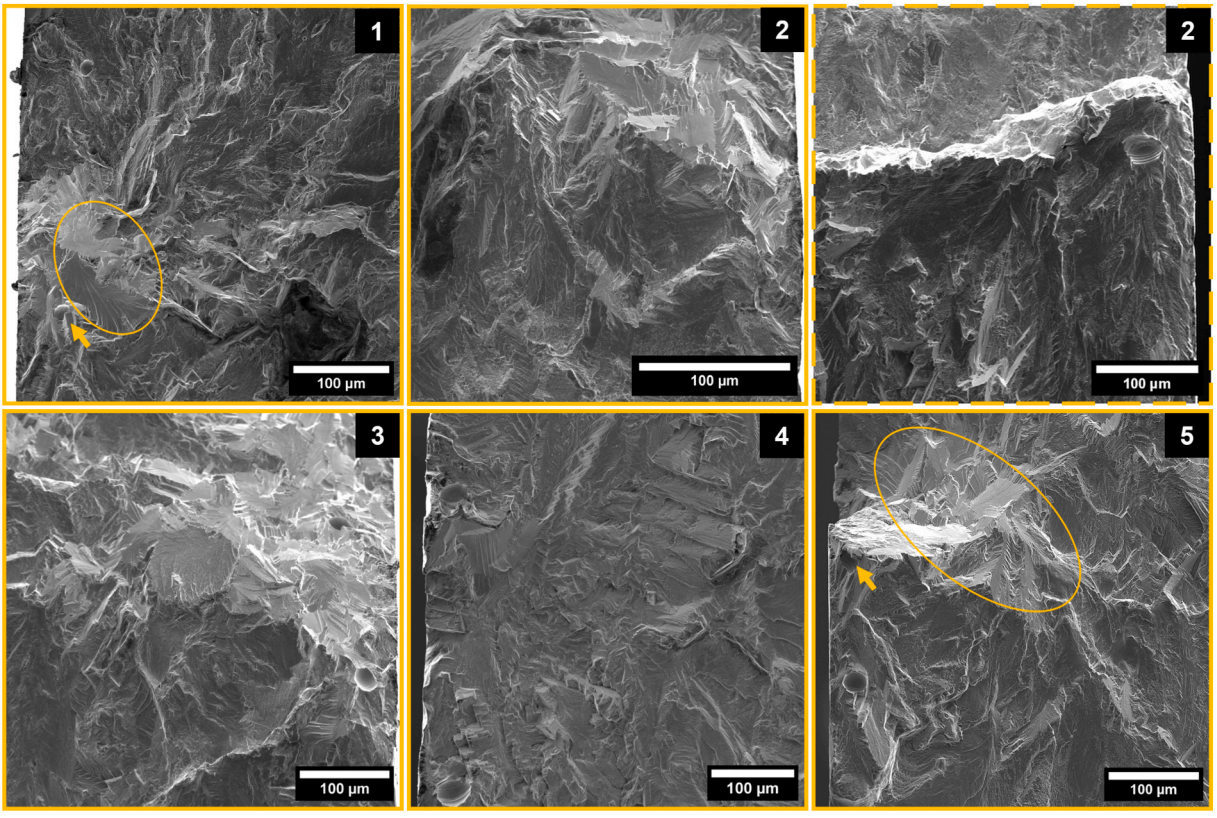


**Fig. 13.** Higher magnification fractographic SEM images showing the fatigue critical features for each sample with outlines corresponding to where they exist in the surfaces shown in Fig. 12.

contouring scan traces the outline of the sample geometry prior to another layer of powder being spread. These porosities are observed to be qualitatively consistent in size and frequency between all sectioned samples and are thus not the cause of the differing fatigue behavior. Quantitative X-ray computed tomography characterization was attempted prior to testing but was unsuccessful in providing contrast necessary to observe keyhole pores due to competing constraints between the thickness of the specimen geometry, necessary voxel size, and the difficulty in penetrating the IN718 microstructure.

The fractured samples and the sectioned fracture surfaces used in the above analysis are shown in Fig. 14. The sample surfaces are all polished up to 400 grit using SiC paper to a near mirror finish. The shiny nature of this surface may appear to be discoloration in the upper image of Fig. 14 but is shown to be an artifact of the photography shown in the lower

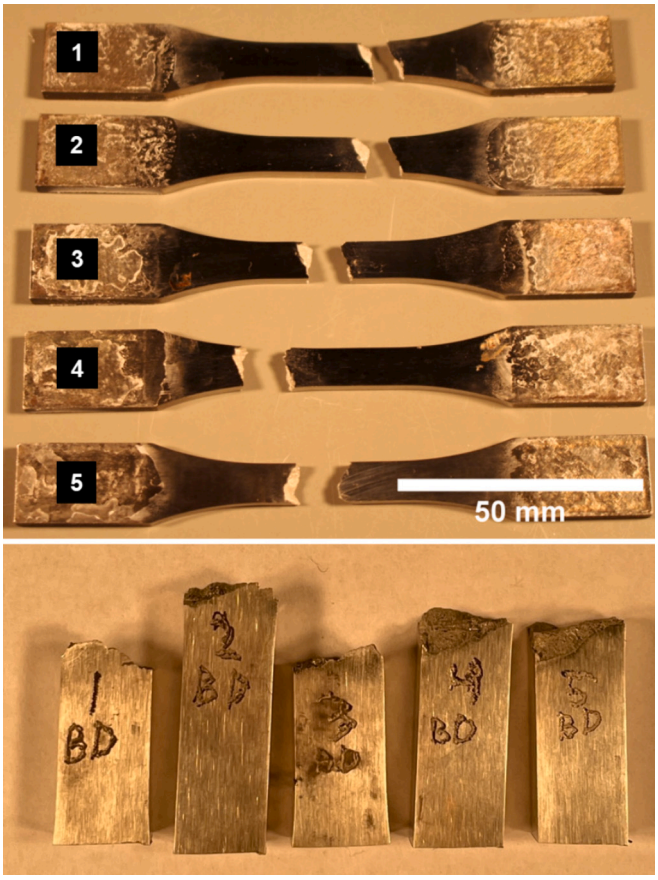


**Fig. 14.** Image showing all fractured samples with the locations of the fatigue failures (upper) and image showing the sectioned fracture surface used in fractography, along with the polished surface finish of all specimens (lower).

image where all sample surfaces are consistent in coloring and finish.

After the fatigue testing and post-mortem fractography, three portions of the gage regions of each sample are mounted to show the orthogonal orientations of the microstructure (XZ, YZ, and XY). All sections are polished following the procedure discussed in Section 2.3 for EBSD analysis. For each sample, six IPF maps are taken from each orientation. A single EBSD map from each orientation is shown in Fig. 15. In all of the XZ and YZ maps, the build direction is positive in the vertical direction, while for the XY maps the build direction is out of the page. In a qualitative analysis of the microstructure of each of the specimens, it can be readily observed that there are large grains extending along the build direction due to the layer wise nature of this LPBF process and the direction of heat flow into the build plate. From a purely qualitative standpoint, there is no microstructural difference readily observable between the different samples. As seen in Fig. 15, there are similar amounts of texturing throughout XZ and YZ faces of all samples with no preferential grain growth observed and likewise observed when comparing all XY orientations. Given the difference in fatigue life between Samples 2, 3, and 4, it is expected that there would be a noticeable qualitative difference in the microstructure, but EBSD characterization reveals that these microstructures appear to be very similar. The only noticeable difference, which can likely be attributed to the sectioning effect, is that the laser tracks are much more observable in the XY orientation of Sample 2 than in any other sample. A rhombohedral grid can be overlaid on this map showing the 67° rotation between layers which is not readily observable in any other sample. Nevertheless, the EBSD images are explored further to extract some quantitative measures of the microstructural texture features, as described in the subsequent section.

### 3.4. Relationships among processing, microstructure, and fatigue life

To quantitatively compare the microstructures of the five samples, the acquired IPF maps from each orientation are further processed by using the ATEX software to measure grain properties including grain area, grain size, and aspect ratio. The mean and standard deviation (Std) of these microstructure features are presented in Table 2. Regarding the mean and standard deviation metrics derived from the microstructure characterizations, Sample 2 shows relatively smaller grain areas in XZ and YZ plane as defined in Fig. 3. It should be noted that the scanning angle in this printing experiment is 67°, which means that neither XZ nor YZ plane captures the transverse section of the melt pool. However, the grain viewed from both the XZ and YZ planes possess an aspect ratio >1.0, as indicated in Table 2. This suggests that the grains formed are primarily columnar due to anisotropic thermal gradients induced by heat extraction (see Section 3.1.2). Sample 2 displays smallest or near smallest grain area, size, and aspect ratio, suggesting a formation of relatively equiaxed grains compared to other samples. This observation provides a clear explanation for the fatigue testing results presented in Table 1, where Sample 2 shows the longest fatigue life (9.30 million cycles). In contrast, Sample 4 exhibits the highest values in most of the grain metrics, signifying the formation of larger and more columnar-shaped grains. This, in turn, elucidates why Sample 4 has the shortest fatigue life (4.00 million cycles) among all the samples. In summary, the quantitative microstructure metrics prove to be valuable in providing accurate and consistent estimations of fatigue strength.

It is worth noting that while Sample 3 also exhibits a relatively shorter fatigue life (4.50 million cycles), the microstructure characterization involves sampling six sections with polished surfaces from each individual whole sample, and these sampled surfaces may not share the same consistency. This phenomenon occurs because the thermal history especially at different heights of the sample could vary significantly due to heat accumulation during the manufacturing process.

Prior research on the effects of processing parameters on the microstructure of LPBF-manufactured IN615 and investigations into the relationship between MP temperatures and grain length for IN718 [37–39] have shown that as the energy density calculated from nominal processing parameters increases, the resulting microstructure tends to display longer grain lengths. With this insight, the ex-situ microstructure characterization results, combined with the in-situ monitored melt pool signatures, provide a comprehensive understanding of the different mechanical properties exhibited by the five samples manufactured under the same condition. As discussed in Section 3.1, the MP temperatures for Samples 3 and 4 are approximately 400 °C higher than those of Samples 1, 2, and 5. When combining the in-situ observed higher MP temperature with the other monitored signatures including larger MP areas, higher counts of spatter ejections, and rougher layer surfaces in Samples 3 and 4, it becomes obvious that these two samples appear abnormal. These samples are confirmed to have lower fatigue lives through our ex-situ testing. It can be concluded from the comprehensive monitoring signatures that the process regime has shifted from the default to keyholing for these two samples, resulting in relatively larger and columnar grains with porosity. The final fatigue lives characterized are results of the combination of microstructure and near-surface porosity. This comprehensive analysis of the interplay between process dynamics, microstructure, and mechanical properties underscores the distinct advantage of possessing multimodal process monitoring capability to evaluate mechanical properties without resorting to expensive and destructive testing methods.

### 3.5. Correlating melt pool, spatter, and layer surface features with fatigue life

To quantify the LPBF process-property relationship, the averages of each in-situ monitored signature for each sample were summarized as shown in Table 3. The reason average signatures are selected in this case

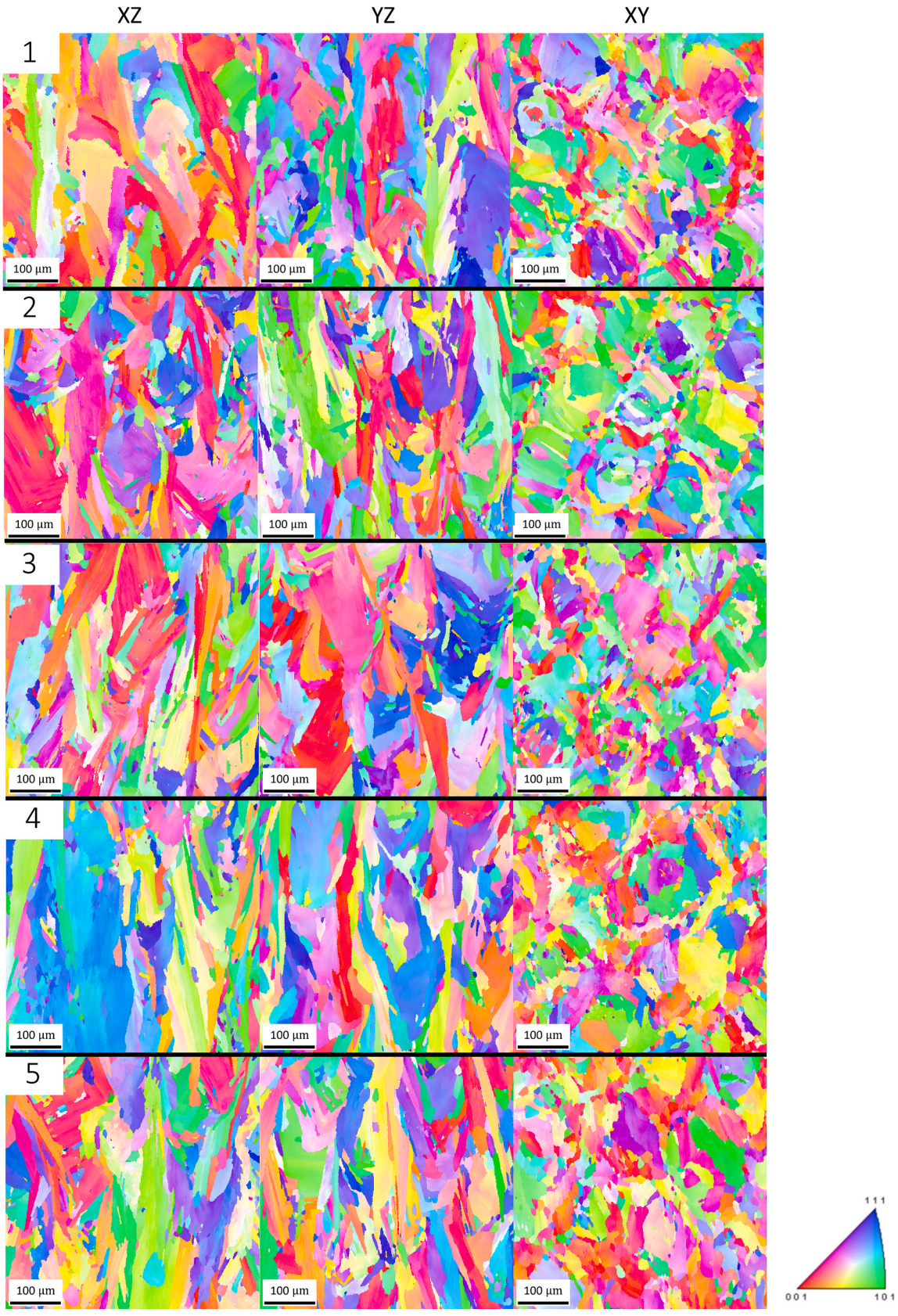


**Fig. 15.** Compilation of EBSD IPF maps of the XZ, YZ, and XY orientations for each of the fatigue samples.

**Table 2**
Mean and standard deviation (Std) of the characterized grain metrics from IPF maps. The maximum and minimum values for each attribute are highlighted with red and blue colors, respectively.

| | Sample 1 | | Sample 2 | | Sample 3 | | Sample 4 | | Sample 5 | |
|---|---|---|---|---|---|---|---|---|---|---|
| | **Mean** | **Std** | **Mean** | **Std** | **Mean** | **Std** | **Mean** | **Std** | **Mean** | **Std** |
| **Grain Area XY ($\mu m^2$)** | 282.97 | 699.93 | 280.25 | 697.64 | **220.75** | **594.29** | **317.00** | **787.96** | 251.85 | 676.17 |
| **Grain Area XZ ($\mu m^2$)** | 438.03 | 1625.3 | **199.55** | **671.92** | 411.01 | 1230.7 | **555.11** | **2075.2** | 555.11 | 2075.0 |
| **Grain Area YZ ($\mu m^2$)** | 387.72 | 1359.5 | **356.68** | **1036.7** | 412.08 | 1282.5 | **464.85** | **1719.7** | 360.67 | 1355.9 |
| **Grain Size XY ($\mu m$)** | 13.52 | 13.32 | 12.72 | 13.96 | **11.65** | **12.06** | **13.87** | **14.54** | 12.81 | 12.52 |
| **Grain Size XZ ($\mu m$)** | 18.39 | 14.81 | **11.45** | **11.09** | 17.37 | 14.89 | **20.59** | **16.82** | 17.84 | 14.20 |
| **Grain Size YZ ($\mu m$)** | 13.79 | 17.42 | 14.59 | **15.53** | 14.88 | 17.42 | **15.74** | **18.55** | **13.16** | 16.91 |
| **Aspect Ratio XY** | 0.96 | 2.069 | **0.89** | **1.99** | 0.99 | 2.07 | 0.93 | 2.08 | **1.05** | **2.12** |
| **Aspect Ratio XZ** | 1.74 | 2.85 | **1.36** | **2.38** | 1.54 | 2.69 | 1.78 | **2.96** | **1.86** | 2.92 |
| **Aspect Ratio YZ** | 1.69 | 2.70 | 1.60 | 2.70 | **1.54** | **2.63** | 1.85 | **3.02** | **1.90** | 2.89 |

**Table 3**
Summary of the input features and output responses (shaded) in process-property correlation modeling. Each input feature is the average of each monitored signature per sample. The average is calculated as the mean of each individual signature across all the monitored layers.

| | Melt pool temperature ($\mathcal{C}$) | Melt pool intensity (au) | Melt pool area ($mm^2$) | $\frac{dT}{dx}$ ($\mathcal{C}/mm$) | $\frac{dT}{dy}$ ($\mathcal{C}/mm$) | $\frac{dT}{dz}$ ($\mathcal{C}/\mu m$) | Spatter Count | Surface Roughness ($\mu m$) | Count of Abnormal Surface Features | Fatigue Life (cycle) | Hardness |
|---|---|---|---|---|---|---|---|---|---|---|---|
| **Sample 1** | 2725.5 | 3205.5 | 0.0306 | 31.30 | 34.36 | 3.22 | 6.0 | 21.97 | 394e3 | 7.12e6 | 491.3 |
| **Sample 2** | 2824.5 | 3204.6 | 0.0312 | 43.53 | 39.53 | 2.89 | 5. 7 | 21.94 | 570e3 | 9.30e6 | 500.4 |
| **Sample 3** | 3241.1 | 3056.9 | 0.0346 | 63.06 | 63.26 | 5.07 | 6.1 | 24.45 | 879e3 | 4.51e6 | 482.8 |
| **Sample 4** | 3166.4 | 3113.6 | 0.0332 | 65.18 | 68.55 | 5.70 | 6.6 | 25.23 | 935e3 | 4.00e6 | 487.2 |
| **Sample 5** | 2806.4 | 3197.9 | 0.0310 | 46.29 | 49.77 | 4.87 | 5.9 | 24.31 | 772e3 | 7.80e6 | 490.2 |

is that it is more representative of the dynamic printing process whereas maximum and minimum are sensitive to noises and outliers. The support vector machine (SVM) regression models are trained to fit the in-situ monitored process signatures to predict the fatigue lives of the manufactured samples. Details of SVM implementation are included in Appendix C. Linear kernel is used as the kernel function to provide a direct measure of feature importance [40]. A total of six models are constructed, each utilizing different combinations of input features. The

selection of features for each model is based on the specific monitoring system used to acquire these features. Generally, the monitoring systems can be categorized into four groups.

1. The conventional coaxial camera monitoring such as infrared camera and optical tomography (Models 1 and 2), which is designed to monitor MP intensity and area.
2. The coaxial imaging pyrometer such as our STWIP (Models 3 and 4), which monitors not only the MP area and intensity profile but also the absolute temperature profile and thermal gradients as reported in Section 3.1.
3. The third monitoring system includes the off-axis high-speed camera for spatter ejection monitoring and the FPP system for layer-wise surface topography measurement (Model 5).
4. The last model (Model 6) integrates all the features monitored through all three monitoring system modalities.

Prior to training, all input features and predictors are normalized to the same scale using z-score normalization. To prevent overfitting, K-fold cross-validation is applied to the training dataset. Given the limited dataset size with five samples, K in this context equals 5. This means the model is trained on 4 samples and validated on 1 sample during each iteration. All the models are coded and implemented using MATLAB, with the random seed for training set sampling fixed to ensure the reproducibility of identical results.

Table 4 shows a comparison of the trained models with mean squared error (MSE), mean absolute error (MAE), and mean absolute percentage error (MAPE) to assess the model's performance. Among the models, Model 6, trained using all of nine process signatures monitored by the three systems, achieves the best performance in predicting fatigue life with a MAPE of 15.00 %. Additionally, Model 5, utilizing only spatter and in-process layer surface features, outperforms Model 1, which represents traditional methods using melt pool imaging intensity features as inputs, but it slightly underperforms Model 2, representing some other traditional methods that combine melt pool imaging intensity and melt pool area. These findings vividly illustrate the pivotal importance of integrating multimodal sensing data in LPBF process-property correlation modeling.

Furthermore, Model 3 and Model 4, trained using signatures derived from our STWIP data, exhibit superior performance in terms of all defined metrics (MSE, MAE, and MAPE) when compared to both traditional models - Models 1 and 2, which are trained using signatures from traditional coaxial camera monitoring. Notably, Model 4, which incorporates the melt pool surface temperature gradients, ranks as the second-best performing model among all the models. This highlights the significance of being able to measure absolute temperature and, consequently, calculate thermal gradients in enhancing the accuracy of fatigue life estimation. As discussed in Section 3.4, the fatigue lives of manufactured samples are influenced by both porosity and microstructure differences resulting from process variations. The melt pool temperature and thermal gradients monitored through coaxial imaging pyrometer, particularly in this case of using the STWIP, effectively reflect processing variation and provide better insights into mechanical properties.

In addition to comparing the feature contributions through training various models, the feature importance of the input signatures is evaluated by extracting the weight coefficients from Model 6 trained with linear kernel. As presented in Fig. 16, the top three most important features obtained from Model 6 are spatter count, thermal gradient in *y* direction, and MP intensity. This indicates that the spatter count carries the most significant weight as the dominant input feature in the regression model. Moreover, the thermal gradient in *y* direction stands out as the second most crucial factor highly correlated to the fatigue lives of LPBF-manufactured samples.

It is important to note that this feature importance study may not provide an entirely accurate reflection of the contributions of different input features due to the limited training data size which restricts the generalizability. However, by combining the results from feature removal/addition, as shown in Table 4, with the estimated feature importance depicted in Fig. 16, we can develop a clear and

**Table 4**
Comparison of Support Vector Model (linear kernel) with different input combinations for predicting fatigue life. The best-performed model is highlighted in green, while the worst-performed model with the worst performance is highlighted in red.

| | Monitoring System | RMSE ↓ (cycle) | MAE ↓ (cycle) | MAPE ↓ (%) |
|---|---|---|---|---|
| **Model 1 (melt pool intensity)** | Conventional coaxial camera | **1.618e6** | **1.506e6** | **27.45** |
| **Model 2 (melt pool intensity, melt pool area)** | Conventional coaxial camera | 1.608e6 | 1.367e6 | 22.99 |
| **Model 3 (melt pool temperature)** | Coaxial imaging pyrometer (STWIP) | 1.568e6 | 1.444e6 | 22.65 |
| **Model 4 (melt pool temperature, melt pool area, melt pool gradients)** | Coaxial imaging pyrometer (STWIP) | 1.434e6 | 1.313e6 | 20.44 |
| **Model 5 (melt pool spatter, in-process layer surface roughness)** | off-axis camera, and FPP | 1.544e6 | 1.408e6 | 23.38 |
| **Model 6 (all 9 input features)** | Coaxial imaging pyrometer (STWIP)FPP, and off-axis camera | **1.153e6** | **9.528e5** | **15.00** |

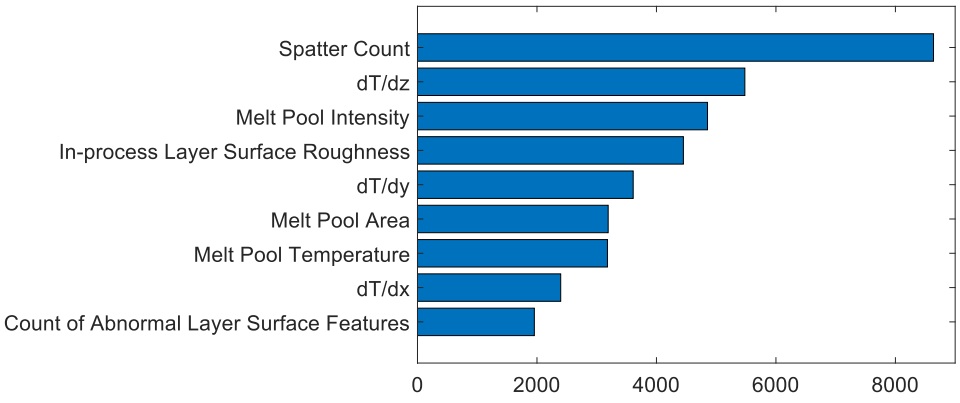


**Fig. 16.** Feature importance of all the inputs used in fatigue life prediction models.

comprehensive understanding of the correlations between in-situ monitored signatures and fatigue lives. Overall, the fatigue life prediction model performs better when a broad range of signatures is used as inputs, emphasizing the critical role of multimodal sensing data fusion in comprehending the correlation between the LPBF process and properties.

### *3.6. Correlating melt pool, spatter, and layer surface features with hardness*

Six SVM regression models, similar to those developed in Section 3.5 for fatigue life prediction, are trained to correlate the in-situ monitored process signatures with the Vickers hardness. Same kernel function and dataset split strategy are implemented to train the hardness correlation models. The six trained models are also categorized based on the monitoring systems deployed for data acquisition in the same way as in Section 3.5. A comparison of these hardness models is shown in Table 5. Model 4, trained using MP temperature, area, and surface temperature gradients, reaches the best performance in predicting HV with a MAPE of 0.81 %. On the other hand, Model 5, which is trained using spatter count and surface roughness, has the highest MAPE of 1.05 %. Overall, all the input signatures monitored can be highly correlated and reach better performance in predicting hardness (≤1 % MAPE) compared to the fatigue life models in previous section (~20 % MAPE). This is potentially due to that the difference in fatigue life across the samples is up to a factor of two, which is significantly larger than the percentage difference in the monitored signatures across the samples (~13 %), as shown in Table 3. Moreover, limited samples and cross-validation settings lead to a relatively large error.

Feature importance analysis for the hardness prediction models was also conducted using the coefficients of the kernel function. As presented in Fig. 17, the top three most important features for the HV prediction model are temperature gradient in *y* direction, count of abnormal in-process layer surface features, and temperature gradient in *x* direction.

**Table 5**
Comparison of Support Vector Model (linear kernel) with different input combinations for predicting Vickers Hardness: the best-performed model is highlighted in green, while the worst-performed model with the worst performance is highlighted in red.

| | Monitoring System | RMSE ↓ | MAE ↓ | MAPE ↓ (%) |
|---|---|---|---|---|
| **Model 1 (melt pool intensity)** | Conventional coaxial camera | 4.3 | 2.7 | 0.55 |
| **Model 2 (melt pool intensity, melt pool area)** | Conventional coaxial camera | 5.0 | 3.3 | 0.68 |
| **Model 3 (melt pool temperature)** | Coaxial imaging pyrometer (STWIP) | 4.9 | 3.9 | 0.78 |
| **Model 4 (melt pool temperature, melt pool area, melt pool gradients)** | Coaxial imaging pyrometer (STWIP) | **4.0** | **2.5** | **0.51** |
| **Model 5 (melt pool spatter, in-process layer surface roughness)** | off-axis camera, and FPP | **6.5** | **5.2** | **1.05** |
| **Model 6 (all 9 input features)** | Coaxial imaging pyrometer (STWIP), FPP, and off-axis camera | 5.4 | 3.9 | 0.78 |

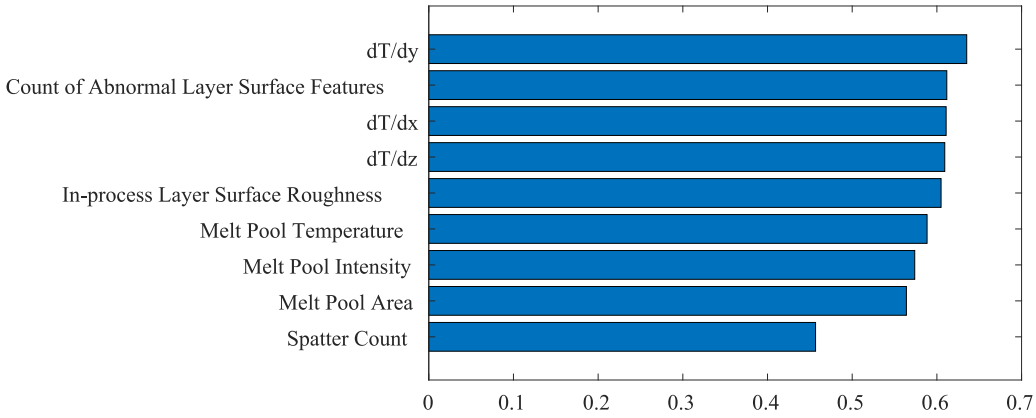


**Fig. 17.** Feature importance of all the inputs used in hardness prediction models,

It is evident that temperature gradients are especially important in both the hardness and fatigue life prediction models. Furthermore, it highlights that the concurrent monitoring of both melt pools and in-process layer surfaces greatly enhances the accuracy of hardness prediction. This once again demonstrates the importance of multimodal multi-sensor monitoring in LPBF for a more accurate modeling of process-property relationships.

As a summary, the regression analyses above effectively demonstrate that in-situ monitored signatures can be significantly correlated with ex-situ properties such as fatigue life and hardness value. Furthermore, the investigation of feature importance and model training with input ablation reveals signatures related to MP temperature, as monitored through coaxial imaging pyrometer (STWIP in this work), play a crucial role capturing process deviations and identifying differences in resulting mechanical properties across various LPBF processes. This holds true even for processes using the same nominal machine setup and processing parameters.

## 4. Conclusions

This research has explored the potential of using in-situ multi-sensor monitoring system to evaluate microstructure and mechanical properties of as-built parts in LPBF. It has demonstrated a framework towards comprehensively evaluating multi-level multimodality process dynamics, microstructure features, and mechanical properties, and establishing their correlations in laser powder bed fusion. The contributions of this work can be summarized as follows:

1. The research has demonstrated a unique in-situ multi-sensor monitoring system and methods, including the coaxial high-speed (30,000 fps) Single Camera Two-wavelength Imaging Pyrometry (STWIP), off-axis camera-based (1000 fps) laser scan and spatter tracking, and Fringe Projection Profilometry (FPP). These methods provide comprehensive measurements of MP intensity, temperature, area, and temperature gradient, spatter count, in-process layer surface roughness, and abnormal layer surface feature count. The system successfully monitored an unprecedented number of layers (43 layers by STWIP, off-axis camera, and FPP) during LPBF experiments of five practical-size fatigue specimens and generated a large amount of multi-sensor data.
2. Experimental results have shown that even under identical processing conditions (default parameters for In718), the actual process, microstructure, and mechanical properties of the samples can vary significantly. All the in-situ monitored signatures listed above exhibited vivid variations, reflecting both stochastic disturbances and systematic deviations in the process. Ex-situ tested properties also displayed differences related to the process variations, with variations in grain sizes, areas, aspect ratios, fatigue life (by a factor up to 2), and hardness values (with an absolute difference of ~10) among the samples.
3. Relationships between the process signatures and outcomes were investigated. In particular, larger MP temperatures and areas, higher counts of spatter ejections, and rougher layer surfaces observed during the printing of Sample 4 align well with its larger and more columnar-shaped grains as well as its lower fatigue lives.
4. Various regression models were trained and compared to quantitatively evaluate the relationships between the LPBF process and mechanical properties. The best-performing models achieved accurate predictions of fatigue life and Vickers hardness, with mean absolute percentage errors of 15 % and 0.51 %, respectively. Melt pool temperature-related features were found to be dominant and can enhance the prediction of mechanical properties, especially when combined with layer surface and/or spatter surface properties.

In summary, this work provides a deeper and more comprehensive understanding of the intricate relationship between multi-level process dynamics, microstructure, and mechanical properties. It emphasizes the significant advantage of having multimodal process monitoring capabilities, enabling the accurate evaluation of microstructural and mechanical properties without the need for costly and destructive testing methods. With an effective multimodal monitoring system, accurate process dynamics can be captured, revealing direct correlations between processing and properties. Furthermore, this work highlights the value of deriving and combining physically meaningful quantities, particularly the measurement of the absolute temperature of melt pools, spatter count, and in-process layer surface roughness, as pivotal factors in predicting part properties. These approaches have proven to be more advantageous than traditional monitoring methods that rely on image intensity-based features. The demonstrated framework of multi-sensor in-situ monitoring and multimodal features fusion will significantly contribute to a comprehensive understanding and closed-loop control of LPBF processes. This approach is crucial for realizing the full potential of LPBF-based additive manufacturing when it comes to producing advanced materials and components with the desired performance characteristics, particularly concerning mechanical strength. Future works include testing the generalizability of the framework on different materials and across different processing parameters. Furthermore, works on incorporating the proposed multimodality melt pool monitoring feedback to control the manufacturing process will be performed.

## CRediT authorship contribution statement

**Haolin Zhang:** Writing – original draft, Visualization, Validation, Software, Methodology, Investigation, Formal analysis, Data curation. **Alexander N. Caputo:** Writing – review & editing, Visualization, Validation, Software, Methodology, Investigation, Formal analysis, Data

curation. **Chaitanya Krishna Prasad Vallabh:** Writing – review & editing, Methodology, Investigation, Formal analysis, Data curation. **Heyang Zhang:** Writing – review & editing, Visualization, Methodology, Investigation, Formal analysis, Data curation. **Richard W. Neu:** Writing – review & editing, Supervision, Resources, Project administration, Methodology, Investigation, Funding acquisition, Conceptualization. **Xiayun Zhao:** Writing – review & editing, Supervision, Resources, Project administration, Methodology, Investigation, Funding acquisition, Conceptualization.

## Declaration of competing interest

The authors declare the following financial interests/personal relationships which may be considered as potential competing interests: Xiayun Zhao reports financial support was provided by U.S. Department of Energy (Award Number: FE0031774) and US National Science Foundation (Award #: 2052662). Xiayun Zhao reports a relationship with University of Pittsburgh that includes: employment. Chaitanya Vallabh reports a relationship with Stevens Institute of Technology that includes: employment. Richard W Neu reports a relationship with Georgia Institute of Technology that includes: employment. Xiayun Zhao and Chaitanya Vallabh are inventors of US Patent 11,874,176, which covers the single-camera two-wavelength imaging pyrometry technology utilized in this paper.

## Acknowledgements

## Funding

This work was supported by the Department of Energy [Grant Number: FE0031774, 2019] and partly supported by the National Science Foundation (NSF) sponsored industry/university cooperative research center (IUCRC) – the Center for Materials Data Science for Reliability and Degradation (MDS-Rely) [Grant Number: 2052662, 2021]. This work also used the National Science Foundation-funded Advanced Cyberinfrastructure Coordination Ecosystem: Services & Support (ACCESS) resource - Pittsburgh Supercomputing Center Bridges GPU and Storage through allocation MCH210015.

Authors would also like to thank 1) ANSYS Additive Manufacturing Research Laboratory (AMRL) at University of Pittsburgh as well as Brandon Blasko for his help with the experiment; 2) Yousra Bensouda for her help with the spatter monitoring images labeling; and 3) Md Mahmudul Hasan for his help with the microstructure imaging data analysis.

## Appendix A. In-situ fringe projection profilometry

### A.1. Three-step phase shifting algorithm and phase to height calibration

The three-step phase shifting method is performed by projecting three sinusoidal patterns to the build area during the printing with phase shift of $0\ \pi$, $\frac{2}{3}\pi$, and $\frac{4}{3}\pi$. The three-step phase shifting algorithm is used to compute the wrapped phase value.

$$I(x,y) = B(x,y) + M(x,y)cos(\phi(x,y) + \delta) \tag{A.1-1}$$

$$I_{Calibrated} = \frac{I_{Camera}}{C_{xy}},\ C_{xy} = \frac{I^{Camera}}{I^{Projected}} \tag{A.1-2}$$

$$\phi(x,y) = arctan\left(\frac{-\sum_{i-1}^{N} I_i^{Calibrated}(x,y)sin(\delta_i)}{\sum_{i-1}^{N} I_i^{Calibrated}(x,y)cos(\delta_i)}\right) \tag{A.1-3}$$

Shown in Eq. (A.1-1), the camera captured intensity at the given pixel location $x$ and $y$ ($I(x,y)$) is the function of ambient background intensity $B$, projector bias $M$, and wrapped phase value $\phi$. $\delta$ is the phase shift of the projected pattern. For FPP system, one major phase error source is from the camera and projector nonlinearity. To account for the nonlinearity between the projected intensity and camera captured intensity, the correction factor $C_{xy}$ is implemented as presented in Eq. (A.1-2). The value of $C_{xy}$ is determined empirically by projecting 20 even-spaced different grayscale intensities from 0 to 255. The two-dimensional Fast Fourier Transform (2D FFT) filter is used to reduce the phase jump error after phase unwrapping stage. In this work, the linear model is used to calibrate the unwrapped phase to height relation [35,41].

### A.2. Phase unwrapping, filtering, and final surface topography

The manual 2D FFT filter is designed to reduce the phase jump error introduced during the phase-unwrapping stage. Shown in Fig. A-1(c), the resulting fused part relative to the powder surface is negative, and the stripe overlapping region presents the relative deeper height value ($\leq -50\ \mu$m) due to the nominal setting of 80 $\mu$m stripe overlapping introducing local heat accumulation. From the height map, the areal surface roughness (Sa), which is the arithmetic mean of the surface deviation from main profile, can be computed as the signature or representation of the layer-wise surface quality.

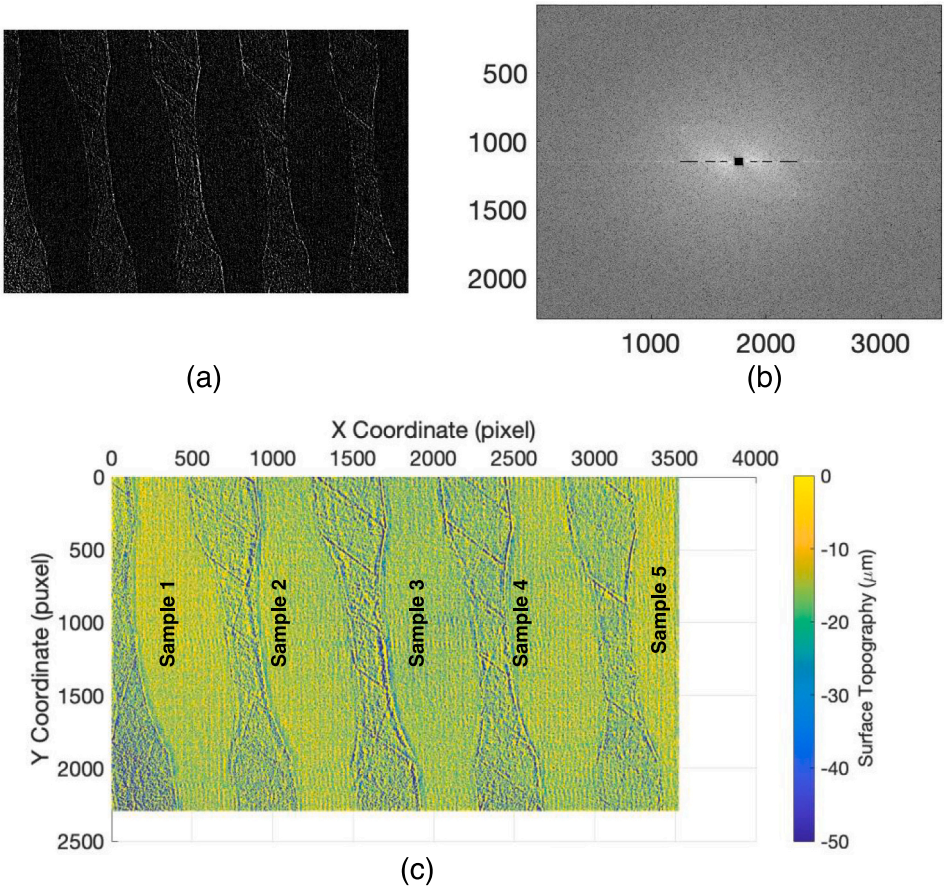


**Fig. A-1.** The application of 2-dimensional Fast Fourier Transform for surface topography filtering. (a) Unwrapped phase map; (b) transformed spectral magnitude diagram, and the filter is applied to the black masked region; (c) final surface topography.

## Appendix B. Unsupervised learning of in-process layer surface topography measurement

In our initial study that aimed to remove the need for effort-taking manual labeling, an unsupervised learning approach was explored, which can automatically categorize pixels from the FPP measured surface topography.

The acquired surface topography is filtered through average pooling followed by the K-means clustering algorithm for detection of local rough pixels. A post-processing check is applied to ensure that the pixels with irregular surface height value (rough feature) are consistent across layers. This automated process allows for rapid data analysis of the 5 fatigue bars. In this case, a simple count of positive rough pixels for each bar is performed. The representative workflow to process layer 14 is shown in Fig. B-1.

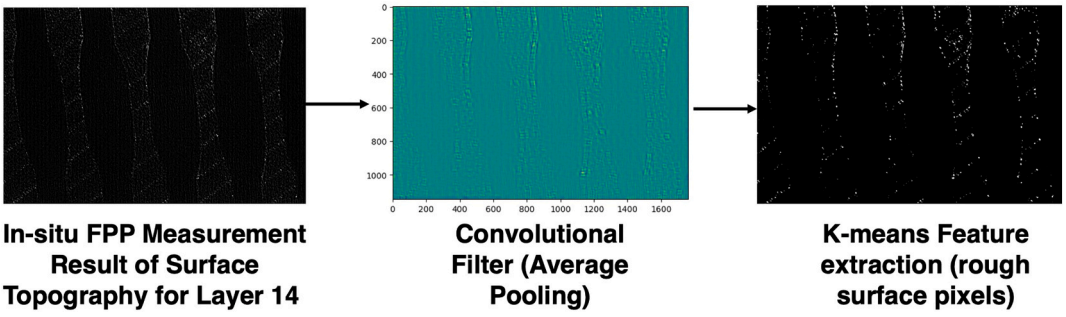


**Fig. B-1.** Feature extraction example for Layer 14 via K-means classification.

As shown in Fig. B-2, the irregular pixels clustered from the k-means algorithm are counted, providing a metric of "Abnormal Surface Feature Count". This metric is correlated with both hardness and high cycle fatigue life which indicates the close correlation between the surface features extracted to the ex-situ characterized mechanical properties. With more abnormal surface features presented in a sample, mechanical properties including hardness and fatigue life degrade correspondingly.

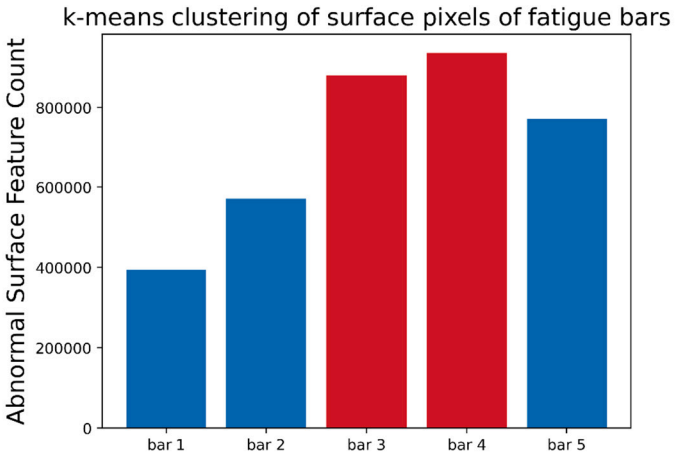


(a)

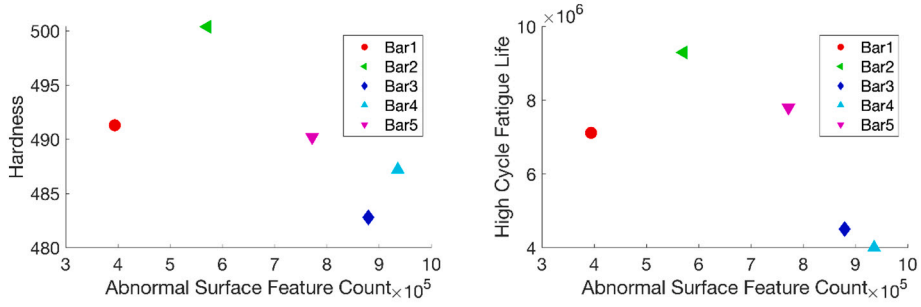


(b) (c)

**Fig. B-2.** Abnormal surface features for the five samples and their correlations to mechanical properties. (a) Abnormal surface feature count for all five samples (b) abnormal surface feature count versus Vickers hardness (c) abnormal surface feature count versus fatigue life.

## Appendix C. Support vector machine regression model

Support vector machine (SVM) is the machine learning algorithm for classification or regression [42,43]. For classification task, the algorithm searches for the optimal hyperplane which maximizes the margin between classes. When performing regression task, the algorithm finds the hyperplane which best fits all the training data.

Specifically, epsilon insensitive SVM ($\varepsilon$-SVM) is implemented in this work through MATLAB statistics and machine learning toolbox. For SVM regression model, the problem is formulated as the optimization problem which a function $f$ with optimized weights $\beta$ and bias $b$ is trained to fit all the training data points $x$.

$$f(x) = \beta x + b \tag{C.1-1}$$

Since the function should be as flat as possible, a convex optimization problem for the weight coefficients $\beta$ can be formulated by minimizing its norms as:

$$J(\beta) = \frac{1}{2}\beta^T\beta \tag{C.1-2}$$

The optimization function $f$ is subjected to the L1 residual ($\varepsilon$) loss function.

$$|y_n - (\beta x + b)| \le \varepsilon, \quad \forall n \text{ training data } 1\ldots n \tag{C.1-3}$$

The specific algorithm is epsilon insensitive which means that all the residual losses less than $\varepsilon$ are ignored which is formally represented as:

$$L_\varepsilon = \begin{cases} 0, \text{ if } |y - (\beta x + b)| \le \varepsilon \\ |y - (\beta x + b)| - \varepsilon, \text{ otherwise} \end{cases} \tag{C.1-3}$$

The optimization problem is solved to find the best fit function for the regression task.

## References


[1] DebRoy T, et al. Scientific, technological and economic issues in metal printing and their solutions. Nat Mater 2019;18(10):1026–32.
[2] Blakey-Milner B, et al. Metal additive manufacturing in aerospace: a review. Materials & Design 2021;209:110008.
[3] Gibson, vol. I., D.W. Rosen, and B. Stucker, Additive manufacturing technologies: 3D printing, rapid prototyping, and direct digital manufacturing. 2nd ed. 2014: Springer-Verlag New York. vol. XXI, 498.
[4] Ramachandiran N, et al. Effects of post heat treatment on microstructure and mechanical properties of Ti5553 parts made by laser powder bed fusion. J Alloys Compd 2023;938.
[5] Leicht A, et al. Effect of process parameters on the microstructure, tensile strength and productivity of 316L parts produced by laser powder bed fusion. Mater Charact 2020;159.
[6] Sehhat MH, et al. Investigation of mechanical properties of parts fabricated with gas- and water-atomized 304L stainless steel powder in the laser powder bed fusion process. Jom 2021;74(3):1088–95.
[7] Gallmeyer TG, et al. Knowledge of process-structure-property relationships to engineer better heat treatments for laser powder bed fusion additive manufactured Inconel 718. Addit Manuf 2020:31.
[8] Ronneberg T, Davies CM, Hooper PA. Revealing relationships between porosity, microstructure and mechanical properties of laser powder bed fusion 316L stainless steel through heat treatment. Materials & Design 2020;189.
[9] Gordon JV, et al. Defect structure process maps for laser powder bed fusion additive manufacturing. Addit Manuf 2020;36:101552.
[10] Khairallah SA, et al. Laser powder-bed fusion additive manufacturing: physics of complex melt flow and formation mechanisms of pores, spatter, and denudation zones. Acta Mater 2016;108:36–45.
[11] Martin AA, et al. Ultrafast dynamics of laser-metal interactions in additive manufacturing alloys captured by in situ X-ray imaging. Materials Today. Advances 2019:1.
[12] Kwabena Adomako N, Haghdadi N, Primig S. Electron and laser-based additive manufacturing of Ni-based superalloys: a review of heterogeneities in microstructure and mechanical properties. Materials & Design 2022;223:111245.
[13] King WE, et al. Laser powder bed fusion additive manufacturing of metals; physics, computational, and materials challenges. Applied. Phys Ther Rev 2015;2(4).
[14] Zhang Q, et al. Estimates of the mechanical properties of laser powder bed fusion Ti-6Al-4V parts using finite element models. Materials & Design 2019;169.
[15] Reijonen J, et al. Cross-testing laser powder bed fusion production machines and powders: variability in mechanical properties of heat-treated 316L stainless steel. Materials & Design 2021;204.
[16] Heckman NM, et al. Automated high-throughput tensile testing reveals stochastic process parameter sensitivity. Mater Sci Eng A 2020;772.
[17] Sing SL, et al. Perspectives of using machine learning in laser powder bed fusion for metal additive manufacturing. Virtual and Physical Prototyping 2021;16(3):372–86.
[18] Bevans B, et al. Heterogeneous sensor data fusion for multiscale, shape agnostic flaw detection in laser powder bed fusion additive manufacturing. Virtual and Physical Prototyping 2023;18(1):e2196266.
[19] Ren Z, et al. Machine learning–aided real-time detection of keyhole pore generation in laser powder bed fusion. Science 2023;379(6627):89–94.
[20] Scime L, Beuth J. Anomaly detection and classification in a laser powder bed additive manufacturing process using a trained computer vision algorithm. Addit Manuf 2018;19:114–26.
[21] Liu Q, et al. Machine-learning assisted laser powder bed fusion process optimization for AlSi10Mg: new microstructure description indices and fracture mechanisms. Acta Mater 2020;201:316–28.
[22] Moorthy S. Modeling and characterization of mechanical properties in laser powder bed fusion additive manufactured Inconel 718. In: Mechanical engineering. Colorado School of Mines; 2018.
[23] Kappes, B., et al., Machine learning to optimize additive manufacturing parameters for laser powder bed fusion of Inconel 718, in Proceedings of the 9th International Symposium on Superalloy 718 & Derivatives: Energy, Aerospace, and Industrial Applications. 2018. p. 595–610.
[24] Liu S, et al. Machine learning for knowledge transfer across multiple metals additive manufacturing printers. Addit Manuf 2021:39.
[25] Gaikwad A, et al. Multi phenomena melt Pool sensor data fusion for enhanced process monitoring of laser powder bed fusion additive manufacturing. Materials & Design 2022;221:110919.
[26] Snow Z, et al. Toward in-situ flaw detection in laser powder bed fusion additive manufacturing through layerwise imagery and machine learning. Journal of Manufacturing Systems 2021;59:12–26.
[27] Feng S, et al. Predicting laser powder bed fusion defects through in-process monitoring data and machine learning. Materials & Design 2022;222.
[28] Gaikwad A, et al. Heterogeneous sensing and scientific machine learning for quality assurance in laser powder bed fusion – a single-track study. Addit Manuf 2020;36:101659.
[29] Elangeswaran C, et al. Predicting fatigue life of metal LPBF components by combining a large fatigue database for different sample conditions with novel simulation strategies. Addit Manuf 2022;50:102570.
[30] Zhang M, et al. High cycle fatigue life prediction of laser additive manufactured stainless steel: a machine learning approach. International Journal of Fatigue 2019;128:105194.
[31] Vallabh CKP, Zhao X. Continuous comprehensive monitoring of melt pool morphology under realistic printing scenarios with laser powder bed fusion. 3D Printing and Additive Manufacturing 2021. https://doi.org/10.1089/3dp.2021.0060.
[32] Vallabh CKP, Zhao X. Melt pool temperature measurement and monitoring during laser powder bed fusion based additive manufacturing via single-camera two-wavelength imaging pyrometry (STWIP). Journal of Manufacturing Processes 2022;79:486–500.
[33] Zhang H, Vallabh CKP, Zhao X. Registration and fusion of large-scale melt pool temperature and morphology monitoring data demonstrated for surface topography prediction in LPBF. Addit Manuf 2022;58:103075.
[34] Zhang H, Vallabh CKP, Zhao X. Influence of spattering on in-process layer surface roughness during laser powder bed fusion. Journal of Manufacturing Processes 2023;104:289–306.
[35] Zhang H, et al. A systematic study and framework of fringe projection profilometry with improved measurement performance for in-situ LPBF process monitoring. Measurement 2022;191:110796.
[36] Lloyd S. Least squares quantization in PCM. IEEE Transactions on Information Theory 1982;28(2):129–37.
[37] Vallabh CKP, et al. Predicting melt pool depth and grain length using multiple signatures from in-situ single camera two-wavelength imaging pyrometry for laser powder bed fusion. J Mater Process Technol 2022;308:117724.
[38] Arısoy YM, et al. Influence of scan strategy and process parameters on microstructure and its optimization in additively manufactured nickel alloy 625 via laser powder bed fusion. The International Journal of Advanced Manufacturing Technology 2017;90(5):1393–417.
[39] Farshidianfar MH, Khajepour A, Gerlich AP. Effect of real-time cooling rate on microstructure in Laser Additive Manufacturing. J Mater Process Technol 2016;231:468–78.
[40] Cortes C, Vapnik V. Support-vector networks. Machine Learning 1995;20(3):273–97.
[41] Zhang H, Prasad Vallabh CK, Zhao X. Machine learning enhanced high dynamic range fringe projection profilometry for in-situ layer-wise surface topography measurement during LPBF additive manufacturing. Precision Engineering 2023;84:1–14.
[42] Vapnik V. The nature of statistical learning theory. Springer Science & Business Media; 2013.
[43] Platt J. Sequential minimal optimization: a fast algorithm for training support vector machines. 1998.